energy could be utilized to drive a thermal reaction which would raise the yield. The photon utilization efficiency could certainly be improved quite dramatically by judicious choice of laser frequency, using high laser fluences, long reaction cells, multiple reflection optics, etc.

The fact that $\langle n_r \rangle$ are comparable for the small and large ester molecules suggests that the laser energy is being more efficiently utilized by the larger molecules. This could be for two reasons: (1) smaller fraction of molecules absorbing the laser energy and (2) greater contribution of post-pulse reaction. We favor the first possibility.

Summary and Conclusions

(1) Extensive data, obtained under carefully controlled conditions, for infrared multiphoton absorption and reaction probabilities have been collected for a series of organic esters. The data for ethyl acetate and ethyl fluoroacetate are believed to be especially reliable and form the basis for detailed modeling studies reported in the accompanying paper.[12]

(2) The extent of collisional energy transfer from excited ester molecules to cold molecules was characterized by adding a small percent of a "thermal monitor". Experiments with a 97:3 ethyl acetate/isopropyl bromide mixture indicated that the reaction probability of isopropyl bromide was much smaller than the reaction probability of ethyl acetate providing the pressure was <0.10 torr. Above 0.10 torr, an increasingly significant fraction of reaction occurred as a consequence of intermolecular energy transfer.

(3) Addition of bath gas reduced the reaction probability significantly, especially at low fluence. Large molecules were more effective deactivators than di- or monoatomic gases, which indicated that the bath gas was causing deactivation of highly vibrationally excited molecules similar to results from chemical activation studies.

(4) Direct and sensitized excitation of *sec*-butyl acetate gave the same product distribution which was independent of ester pressure and laser fluence. Direct and sensitized excitation of ethyl

2-bromopropionate gave similar results, indicating that vibrational energy randomization precedes chemical reaction for direct excitation.

(5) Bulk laser absorption cross sections, σ_L, vs. ϕ, were measured for six esters. The cross sections were independent of pressure but were mildly dependent on fluence. At low fluence, ~0.1 J cm^{-2}, the laser cross section had the same value as the broad-band cross section at the same frequency.

(6) A plot of log $P(\phi)$ vs. log ϕ showed approximately linear behavior for $P(\phi)$ values of 10^{-2} to 10^{-4} with slopes of 4–6 reflecting the strong dependence of the reaction probability on fluence. At fluences $\gtrsim$4 J/cm^2 the $P(\phi)$ curve asymptotically approached constant values, usually between 0.5 and 1.0.

(7) Plots of $P(\langle n \rangle)$ vs. the average number of absorbed photons, $\langle n \rangle$, for ethyl acetate and ethyl fluoroacetate demonstrated that *the reaction probability for the same amount of absorbed energy was dependent on laser frequency*. This was interpreted as showing that only a certain fraction of molecules, rather than all molecules within the irradiated volume, absorb the laser energy to produce a two- (or greater) component energy distribution. This fraction probably is fluence dependent. The situation may occur for the other molecules too, even though it was definitely shown only for ethyl acetate and ethyl fluoroacetate.

(8) The reaction probability of ethyl acetate irradiated at P(20) was very dependent on pressure for constant $\langle n \rangle$, indicating an enhancement of yield because of thermal contributions at higher pressures. For excitation with P(38) the pressure effect for constant $\langle n \rangle$ was less significant because the laser-driven component was much larger than for P(20) experiments.

Multiphoton Laser-Induced Chemistry of Organic Esters: Comparison with Master Equation Calculated Results

J. C. Jang, D. W. Setser, and Wayne C. Danen*

Contribution from the Department of Chemistry, Kansas State University, Manhattan, Kansas 66506. Received April 16, 1981

Abstract: A master equation formulation without bottlenecks has been used to examine some general and specific features of the CO$_2$ laser-induced unimolecular reactions of organic esters (experimental studies are presented in the preceding paper). The general features should apply to other large molecules having a reaction threshold near 45 kcal mol^{-1} and comparable absorption cross section. The incubation period and postpulse phenomena that are (or can be) very important in bulb experiments for large molecules are illustrated by calculation. For exoergic or mildly endoergic reactions a postpulse bulk cooling wave is important for limiting the extent of reaction. The specific features include assignment of level-to-level absorption cross sections and comparison of experimental and calculated reaction probabilities for ethyl acetate and ethyl fluoroacetate excited at two different wavelengths. The calculations, which include postpulse collisions, reproduce the general trends in the data. Nearly quantitative agreement is obtained in the steady-state (high fluence) regime. The calculations generally underestimate the reaction probability at low fluence, and the discrepancy is especially serious for ethyl acetate and ethyl fluoroacetate at the P$_{38}$ and P$_{10}$ frequencies, respectively. These deficiencies can be rationalized by assuming that only a certain fluence-dependent fraction of the molecules participate in multiphoton absorption. Experimental data and calculated results also are given for excitation of ethyl fluoroacetate in He and CF$_4$ buffer gas.

I. Introduction

The preceding paper[1] reported the reaction probabilities of organic esters for a given absorbed CO$_2$ laser energy. In the present paper, master equation computations are done to provide

insight into the physical and chemical processes resulting from CO$_2$ laser irradiation of the organic esters. The experimental constraints to the model are the reaction probabilities and the absorbed laser energy for a wide range of laser fluences. The master equation was formulated assuming that (i) the ester molecules are in the quasi-continuum region, even at room temperature, (ii) RRKM unimolecular rate constants describe the

(1) Danen, W. C.; Rio, V.; Setser, D. W. *J. Am. Chem. Soc.*, preceding paper in this issue.

variation of rate constant with energy, and (iii) collisions during the pulse can be ignored (for experimental conditions of our work). At the reaction threshold energy the RRKM rate constants are small ($k_i = 9.5 \times 10^1$, 1.0×10^3, and 6.0×10^3 s^{-1} at 5, 10, and 15 kcal mol^{-1} excess energy for ethyl acetate), and postpulse considerations (collisional deactivation, thermal reaction, and bulk cooling) must be considered for bulb experiments. These features are considered when comparing the experimental and calculated reaction probability. Our objective is twofold. First, we explore the consequences of multiphoton excitation for a model that uses RRKM rate constants and has no bottleneck limitations in the multiphoton absorption process and identify relationships between experimental variables and parameters of the model. In the second stage, the correspondence between the calculated and the experimental reaction probability is examined. Some new experimental data for ethyl acetate and ethyl fluoroacetate also are reported. These consist of reaction probability measurements of ethyl fluoroacetate at constant pressure of CF_4 (0.7 and 1.5 torr) and He (3.5 torr) vs. fluence. These data are somewhat easier to model than measurements of the reaction probability, $P(\phi)$, vs. pressure of bath gas at constant laser energy fluence, ϕ, which were given in the preceding paper.[1]

Our use of the master equation resembles the approach of Lyman[2] and of Lee et al.[3] for SF_6 or Moore et al. for C_2H_5Cl.[4] The most uncertain features are the fraction of molecules participating in incoherent excitation and the level-to-level absorption cross sections. We have used cross sections that are based on the energy absorption measurements and assumed that *all* molecules in the irradiated volume have the same absorption cross sections. The *true* fraction of molecules that absorbs energy and the dependence of this fraction on fluence are crucial questions and play a critical role in assessing more subtle effects, such as intramolecular rates of energy relaxation. However, the reaction probabilities of the esters are large[1,5] and a high fraction of molecules must participate in multiphoton absorption. Thus, assuming that all molecules, regardless of the rotational or vibrational state in the thermal ensemble, have the same cross section is the simplest reasonable assumption. The physical basis of why ethyl acetate should closely follow such a model is considered in the Discussion.
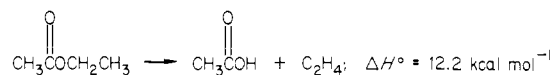
II. Master Equation Formulation

The vibrational energy region was divided into equally spaced levels; each level has a degeneracy proportional to the vibrational density of states at the mean energy. A rate equation is written for the population, N_i, of each level which accounts for single-photon stimulated absorption and emission, unimolecular reaction, and collisional energy transfer:

$$dN_i/dt = I(t)[\sigma_{i,i-1}N_{i-1} + \sigma_{i,i+1}N_{i+1} - (\sigma_{i+1,i} + \sigma_{i-1,i})N_i] + \omega\sum_j P_{ij}N_j - \omega N_i - k_iN_i \quad (1)$$

The microscopic cross section for transfer from level i to $i + 1$ by absorption of laser energy is $\sigma_{i+1,i}$ and is related to $\sigma_{i,i+1}$ by detailed balance, i.e., $\sigma_{i,i+1} = (g_i/g_{i+1})\sigma_{i+1,i}$, where g_i is the degeneracy or vibrational density of states of level i. The collision frequency is ω, P_{ij} is the collisional transition probability from level j to i, k_i is the RRKM unimolecular rate constant, and $I(t)$ is the laser intensity in units of photons cm^{-2} s^{-1}.

Ethyl acetate undergoes a unimolecular transformation to molecular products with a threshold energy of 47 kcal mol^{-1}.

$$CH_3\overset{O}{\overset{\|}{C}}OCH_2CH_3 \longrightarrow CH_3\overset{O}{\overset{\|}{C}}OH + C_2H_4; \quad \Delta H° = 12.2 \text{ kcal mol}^{-1}$$

The average vibrational energy at 300 K is 980 cm^{-1} and the vibrational state density is ~4 and ~120 states cm^{-1} at 980 and 2000 cm^{-1}. The rotation state density ($I_A = 94.5$, $I_B = 422$, I_C

$= 500 \times 10^{-40}$ g cm^2) at room temperature is ~600 states cm^{-1}. In doing the master equation calculations, the 300 K distribution was placed into the $i = 0$, 1, and 2 levels with relative population of 0.76, 0.21, and 0.03. The omission of rotational levels from the model means that specific transitions from initial to final rotational states are being ignored. An important point is that the reaction is only slightly endothermic and the energy deposited in the irradiated volume remains as kinetic energy (heat) rather than being converted to chemical potential energy. Realistic transition-state models are used for the RRKM calculations (see Appendix I) and the k_i values should be good to a factor of $\lesssim 3$. The level separation normally was taken to be the laser photon energy, 1050 cm^{-1} or ~3 kcal mol^{-1}; however, a finer grain of 1 kcal mol^{-1} spacing was used for some exploratory calculations. The harmonic density of states were calculated from molecular frequencies (Appendix I). Empirical level-to-level cross sections with a dependence on vibrational energy that reproduces the variation of the total absorption cross section with laser fluence will be used. They are not state-to-state cross sections since each of our levels contains many states.

Realistic estimates[6] can be made for the collisional transition probabilities for collisions between a polyatomic molecule with vibrational energy in excess of ~30 kcal mol^{-1} and a bath gas molecule at 300 K. Treating the collisional processes for the lower levels, which may involve specific quantum states, becomes more difficult. Fortunately, collisions with the lower levels are less important if the laser pulse is shorter than time between collisions. Our laser pulse consists of a ~130-ns spike followed by a ~1.2-μs tail, and for 0.05-torr experiments collisions during the laser pulse are negligible. However, collisions do introduce complicated postpulse phenomena for bulb experiments (postpulse phenomena will be discussed in section IV). For experiments with added inert bath gas, collisional processes involving the lower levels should be considered during the IR absorption processes and this also is considered in section IV. In the following section, the multiphoton absorption processes will be considered under collisionless conditions.

III. Calculated Collisionless Results for Ethyl Acetate

1. **Formulation of the Model.** Under collisionless conditions, eq 1 reduces to

$$\frac{dN_i}{dt} = I(t) \times$$
$$\left[\sigma_{i,i-1}N_{i-1} + \frac{g_i}{g_{i+1}}\sigma_{i+1,i}N_{i+1} - \left(\sigma_{i+1,i} + \frac{g_{i-1}}{g_i}\sigma_{i,i-1}\right)N_i\right] - k_iN_i \quad (2)$$

If unimolecular dissociation is not important during the laser pulse, eq 2 becomes

$$\frac{dN_i}{I(t)\,dt} = \frac{dN_i}{d\phi} =$$
$$\sigma_{i,i-1}N_{i-1} + \frac{g_i}{g_{i+1}}\sigma_{i+1,i}N_{i+1} - \left(\sigma_{i+1,i} + \frac{g_{i-1}}{g_i}\sigma_{i,i-1}\right)N_i \quad (3)$$

and the vibrational energy distribution is dependent only on the laser fluence ($I(t)\,dt$).

Consider first the situation if $k_i = 0$ (see eq 3). The average number of photons absorbed per molecule, $\langle n \rangle$, is given by the integral of eq 4 over time. Substituting dN_i/dt from eq 3 into

$$\frac{d\langle n \rangle}{dt} = \frac{1}{N}\sum_{i=1}(i - 1)\frac{dN_i}{dt} \quad (4)$$

eq 4 gives eq 5, where $\sigma_i' = \sigma_{i+1,i} - \sigma_{i-1,i}$ is the net cross section per level. If σ_i' is constant, $d\langle n \rangle h\nu/d\phi = \sigma'$ and $\langle n \rangle h\nu = \omega'\phi$; therefore, the absorbed energy per molecule will be linearly dependent on the laser fluence with the proportionality constant σ'. However, for real molecules σ' will not be constant. In this section

(2) Lyman, J. L. *J. Chem. Phys.* **1977**, *67*, 1868.
(3) Schulz, P. A.; Sudbo, Aa.S.; Grant, E. R.; Shen, Y. R.; Lee, Y. T. *J. Chem. Phys.* **1980**, *72*, 4985.
(4) Dai, H. L.; Kung, A. H.; Moore, C. B. *J. Chem. Phys.* **1980**, *73*, 6124.
(5) Danen, W. C.; Jang, J. C. "Laser Induced Chemical Processes"; Steinfeld, J. I., Ed.; Plenum: New York, 1981; Vol. I.

(6) (a) Tardy, D. S.; Rabinovitch, B. S. *Chem. Rev.* **1977**, *77*, 369. (b) Marcoux, P. J.; Setser, D. W. *J. Phys. Chem.* **1978**, *82*, 97. (c) Richmond, G.; Setser, D. W. *Ibid.* **1980**, *84*, 2699.

5442 *J. Am. Chem. Soc., Vol. 104, No. 20, 1982*

Jang, Setser, and Danen

$$\frac{d\langle n\rangle}{I dt} = \frac{d\langle n\rangle h\nu}{d\phi} = \frac{1}{N}\left[\sigma_{21}N_1 + \left(\sigma_{32} - \frac{g_1}{g_2}\sigma_{21}\right)N_2 + \right.$$

$$\left. \ldots \left(\sigma_{n+1,n} - \frac{g_{n-1}}{g_n}\sigma_{n,n-1}\right)N_n + \ldots\right] =$$

$$\frac{1}{N}[\sigma_1'N_1 + \sigma_2'N_2 + \sigma_3'N_3 + \ldots + \sigma_n'N_n + \ldots] \quad (5)$$

the consequences of different types of cross sections upon observable experimental quantities are examined. For different sets of cross sections the average number of photons absorbed per molecule, $\langle n\rangle$, will be compared with F_R (fractional yield at the termination of laser pulse) and F_R^∞ (the sum of F_R and the fraction of molecules above E_0, the reaction threshold energy). F_R^∞ corresponds to the total fractional reaction yield for collisionless conditions.

2. Cross Sections, Absorbed Energy, and Distribution Functions. Four different sets of microscopic section, $\sigma_{i+1,i}$, were examined. The four cases are described in terms of the broad-band cross section, σ_{10}, which is 3.3×10^{-19} cm²: (a) $\sigma_{i+1,i} = \sigma_{10}$, (b) $\sigma_{i+1,i} = \sigma_{10}(i + 1)^{1/2}$, and (c) $\sigma_{i+1,i} = \sigma_{10}/(i + 1)^{1/2}$. Models a–c include stimulated emission but case d, $\sigma_{i+1,i} = \sigma_{10}$ with $\sigma_{i,i+1} = 0$, also was examined for reference. The $\sigma_{i,i+1}/\sigma_{i+1,i}$ ratios are governed by g_i/g_{i+1}, which are 0.24, 0.32, 0.46, 0.50, and 0.60 at 30, 48, 80, 100, and 140 kcal mol⁻¹, respectively. The $\langle n\rangle$ values were calculated for a 300-ns rectangular pulse using eq 2 for the four models. The pulse shape has little influence on these calculated results and the results shown in Figures 1–4 have general validity for a given fluence. For constant $\sigma_{i+1,i}$ but with stimulated emission (case a), the slope of the $\langle n\rangle$ vs. ϕ plot is reduced relative to case d. If σ_i' increases (case b) or decreases (case c) with energy, the slope of the $\langle n\rangle$ vs. ϕ increases or decreases, respectively, with ϕ. This can be easily seen by inspection of the calculated bulk laser absorption cross section, $\sigma_L(\phi)$ vs. ϕ plot (Figure 1). $\sigma_L(\phi)$ was obtained from $\sigma_L(\phi) = \langle n\rangle h\nu/\phi$ for a given ϕ. Since σ_i' is constant for case d, $\sigma_L(\phi)$ is independent of ϕ, providing that molecules are not removed by reaction during the pulse. The calculations shown in Figure 1, in fact, include unimolecular reaction, and the deviation between the dotted and solid lines is a consequence of unimolecular reaction of ethyl acetate during the laser pulse. Indeed, the calculated $\sigma_L(\phi)$ for case d is constant up to $\phi \sim 1.2$ J cm⁻² for which $F_R = 4.4 \times 10^{-3}$ (even though F_R^∞ is 0.85); at 2.0 J cm⁻² $F_R = 0.32$ and $\sigma_L(\phi)$ is significantly reduced. The $\sigma_L(\phi)$ for the constant $\sigma_{i+1,i}$ model, but including stimulated emission (case a), systematically decrease even though the reaction during the pulse is negligible ($F_R = 0.039$ at 2.0 J cm⁻²). The $\sigma_L(\phi)$ for case b rapidly rises and $\sigma_L(\phi) \approx 2\sigma_{10}$ at $\phi \sim 0.4$ J cm⁻². An even larger increase would result, except for depletion of molecules during the laser pulse (at 0.6 J cm⁻² $F_R = 0.059$ and $F_R^\infty = 0.82$; at 0.8 J cm⁻² $F_R = 0.39$ and $F_R^\infty = 0.97$). For case c $\sigma_L(\phi)$ declines more rapidly than for case a, and $\sigma_L(\phi) \approx \frac{1}{2}\sigma_{10}$ at $\phi \sim 0.5$ J cm⁻²; F_R is negligible for $\phi \le 3$ J cm⁻², and for case c the fall in $\sigma_L(\phi)$ is strictly a consequence of the functional form of $\sigma_{i+1,i}$. Fluences of >3 J cm⁻² are required for F_R to be significant for case c.

Two conclusions arise from these calculations. (i) Information about the form of the microscopic cross sections can be deduced from measurements of $\sigma_L(\phi)$. (ii) For $F_R \gtrsim 0.05$, $\sigma_L(\phi)$ declines from loss of molecules by unimolecular reaction. The experimental[1] $\sigma_L(\phi)$ generally resemble (a) or (d) of Figure 1. However, for some examples, usually for wavelengths to the red of the band maximum, the dependence of $\sigma_L(\phi)$ resembles (b).

The time evolution of the absorbed energy and the fractional reaction at time t, F_t, is shown in Figure 2 for models a and b. Even if $\sigma_{i+1,i}$ increases with energy, (model b), ~ 100 ns is required for acquisition of enough energy to give appreciable reaction during the pulse. This is true even if F_R^∞ is extensive; see Figure 3. At the same ϕ, longer times are required for onset of reaction with model a than with model b. At low-energy fluences or in the threshold regime, the incubation time,[7,8] i.e., the time delay be-
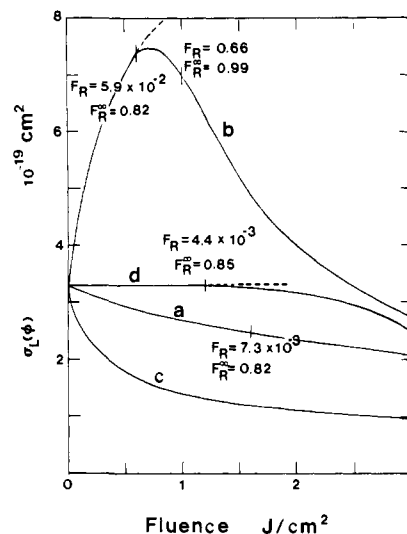

Figure 1. Variation of the laser absorption cross section, $\sigma_L(\phi)$ vs. laser fluence, ϕ, for four cross-section models: (a) $\sigma_{i+1,i} = \sigma_{10}$, (b) $\sigma_{i+1,i} = \sigma_{10}(i + 1)^{1/2}$, (c) $\sigma_{i+1,i} = \sigma_{10}/(i + 1)^{1/2}$, (d) $\sigma_{i+1,i} = \sigma_{10}$; $\sigma_{i,i+1}$ is given by microscopic reversibility for (a), (b), and (c), but $\sigma_{i,i+1} = 0$ for (d). Calculations were done with eq 2 for a 300-ns rectangular laser pulse and $\sigma_{10} = 3.3 \times 10^{-19}$ cm²; the broken lines show the results if unimolecular reaction is supressed, i.e., $k_i = 0$. F_R and F_R^∞ are cited at several ϕ to illustrate the onset of the decline in $\sigma_L(\phi)$ due to unimolecular reaction. The decline in $\sigma_L(\phi)$ for (d) is entirely due to unimolecular reaction; the abrupt break in $\sigma_L(\phi)$ for (b) at $\phi \sim 0.6$ J cm⁻² and the subsequent strong decline also is a consequence of unimolecular reaction.
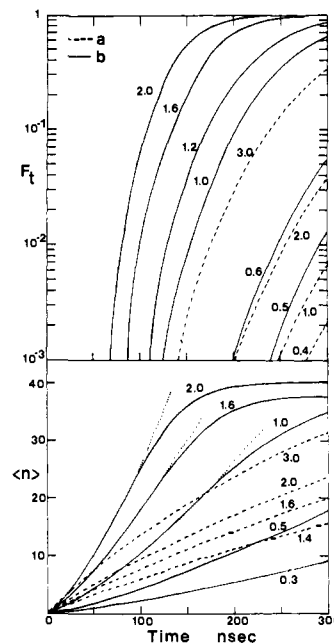

Figure 2. Plot of F_t and $\langle n\rangle$ vs. time for variable fluences for cross-section models (a) (---) and (b) (—) of Figure 1; $\langle n\rangle$ is the mean number of absorbed photons. The calculations are for collisionless conditions with a 300-ns rectangular pulse. The dotted extensions of the 2.0, 1.6, and 1.0 J cm⁻² curves of model b in the lower panel are results without unimolecular reaction. Energy fluences (J cm⁻²) are indicated by the numbers.

tween the onset of the laser pulse and start of product formation, may be significant. The incubation time, t_{inc}, as a function of the laser intensity, I, can be expressed analytically for the constant net cross-section case (case d)[9] and is directly proportional to I^{-1}. No simple relation describes the other cross-section models; t_{inc} will decrease as I^{-s} with $s > 1.0$ for case b and $s < 1.0$ for cases a and d. However, our numerical calculations[9] for t_{inc} (defined

(7) Yahav, G.; Haas, Y. *J. Chem. Phys.* **1980**, *72*, 3410.

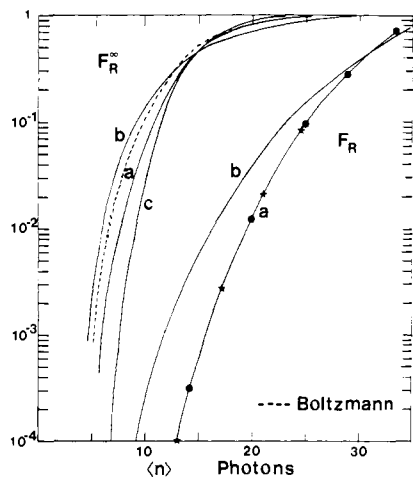(8) Troe, J. *J. Chem. Phys.* **1980**, *73*, 3205.

Laser-Induced Chemistry of Organic Esters

J. Am. Chem. Soc., Vol. 104, No. 20, 1982 5443

Figure 3. Plot of F_R and F_R^∞ vs. $\langle n \rangle$ for models a and b. Calculations are for collisionless conditions and a 300-ns rectangular pulse (eq 2). The points on the (a) F_R curve are: ●, $\sigma_{10} = 3.3 \times 10^{-19}$ cm²; ★, $\sigma_{10} = 0.66$ ×| 10^{-19} cm². A higher fluence is required to obtain for the latter the same $\langle n \rangle$; see text. For comparison, the F_R^∞ values for model c and for a Boltzmann distribution (- - -) of the same mean energy are also shown. To obtain the total mean energy the $\langle n \rangle$ values should be increased by ~1 unit to account for the initial thermal energy.

as the time for $F_t = 10^{-3}$ vs. I^{-1} for models a and b showed that the deviations from the linearity were very small, although the slopes of the t_{inc} vs. I^{-1} plots were very dependent on the microscopic cross sections. If t_{inc} is longer than the laser pulse length, the reaction yield will be entirely dominated by postpulse phenomena. The postpulse phenomena will be discussed in section III.4.

In addition to the general features, an important point of Figure 2 is the break in the $\langle n \rangle$ vs. time plots for 1.6 and 2.0 J cm⁻² at $F_R \sim 0.05$ ($t \sim 100$ ns) for case b; these correspond to the onset of reduced absorption because of reaction during the pulse. As a final point of Figure 2, note the lesser extent of reaction for case a at 3.0 J cm⁻² relative to case b at 1.0 J cm⁻² even though $\langle n \rangle$ is larger for the former during the first 160 ns. Thus, the dependence of the microscopic cross sections on energy can affect F_R even for nearly the same $\langle n \rangle$. Figure 3 further illustrates this in a plot of F_R and F_R^∞ vs. $\langle n \rangle$. The dependence of F_R on the microscopic cross sections is pronounced for low $\langle n \rangle$; case b gives higher F_R and F_R^∞ than case a and broader energy distribution (see Figure 4). However, the dependence of F_R^∞ upon the microscopic cross sections is relatively small for $\langle n \rangle \geq 10$. Two model a calculations were done with the same dependence of $\sigma_{i+1,i}$ on energy, but with $\sigma_{10} = 3.3$ and 0.66×10^{-19} cm². Figure 3 shows that F_R is the same for the two σ_{10} at the same $\langle n \rangle$, which is expected since the $\sigma_{i+1,i}$ values are related by a constant. However, to obtain the same $\langle n \rangle$ for two different σ_{10}, a higher ϕ is required for the smaller σ_{10}. This illustrates the advantage of comparing the reaction yields vs. $\langle n \rangle$ rather than vs. ϕ.

Figure 4 shows the vibrational distributions at the end of the laser pulse corresponding to absorption of energy equivalent to ~13.5 photons for cases a, b, and c and ~22 and ~30 photons for cases a and b; these are compared with Boltzmann distributions of the same average energy (dotted curves). The initial thermal vibrational energy increases the average energy by about one photon, and a laser-induced distribution characterized by absorption of $\langle n \rangle$ photons should be compared to a Boltzmann distribution of $\langle E \rangle = (\langle n \rangle + 1)h\nu$. According to Figure 3, $\langle n \rangle$ = 13.5 and 22 correspond to $F_R < 10^{-3}$ and ~0.05, respectively, and depletion by chemical reaction is negligible. The distributions broaden in the series c < a < b, but only the case b distribution (increasing $\sigma_{i+1,i}$ with energy) for $\langle n \rangle$ = 13.5 is broader than an equivalent Boltzmann distribution. For $\langle n \rangle$ = 30, F_R is quite significant and depletion of the high-energy part of the distributions
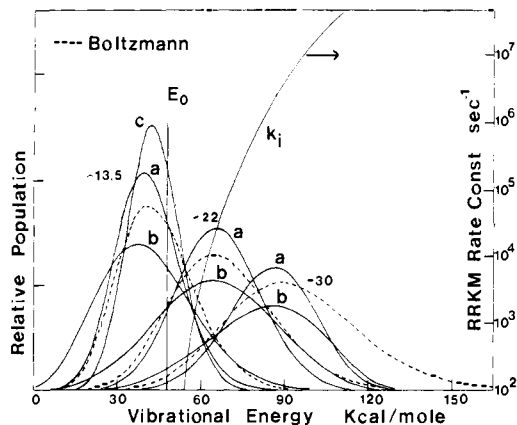

Figure 4. Distribution functions at the termination of the laser pulse for a common $\langle n \rangle$ of ~13.5, 22, and 30 for cross-sections models a, b, and c from eq 2 with the 300-ns rectangular pulse. The Boltzmann distributions of the same mean energy (- - -) are shown for comparison. The RRKM rate constant, k_i, values for ethyl acetate also are shown. E_0 is the reaction threshold energy for ethyl acetate.

in Figure 4 is evident. As $\langle n \rangle$ becomes larger, F_R increases until most of the reaction occurs during the pulse, and eventually the reaction rate will be in steady state[10] with the laser pumping rate. The steady state is discussed in the next section and more fully in Appendix II.

The rather small apparent differences in the high-energy tails of the distributions resulting from different $\sigma_{i+1,i}$ models can combine with the rapidly increasing RRKM rate constants with energy to give a significant dependence of F_R on the cross-section model. However, the variation in F_R^∞ with model is not so strong, and F_R^∞ = 0.1 corresponds for $\langle n \rangle$ = 10.5–11.5 for all three models. For $F_R \leq 0.1$, a Boltzmann distribution defined by $\langle n \rangle$ + the thermal energy is a reasonable approximation to the vibrational distribution for molecules that follow eq 1 and have $\sigma_{i+1,i}$ values represented by models a–c. This conclusion will need some modification if collisions occur during the pulse; collisions lower the mean energy and broaden (to low energy) the distribution.

3. Reaction Probability vs. Time, Intensity, Fluence, and $\langle n \rangle$. Inspection of a F_t vs. time plot (Figure 2 and Appendix II) suggests that the discussion can be divided into a threshold regime, an intermediate regime, and a steady-state regime. These regimes also can be defined in terms of $\langle n \rangle$ or ϕ for fixed time experiments. In the threshold regime some molecules have been transported above E_0; however, $\langle n \rangle$ is sufficiently low that very little reaction occurs during the pulse and F_R is $10^{-3} - 10^{-4}$. For large molecules, a large fraction may be above E_0 and the system may still be in the threshold regime because the rate constants are small and the incubation time is so long that virtually all reaction occurs after the pulse. For these conditions a model in which the average absorbed energy is used to describe an equivalent vibrational Boltzmann distribution and the reaction yield is calculated from the competition between the collective deactivation processes, and unimolecular reaction is a reasonable approximation.[5] This point of view is basically the formation advocated by Yablonovitch and co-workers[11] and by others.[12] If this formation is used outside the threshold regime, F_R must be added to the post-pulse yield.

A detailed analysis of the steady-state regime is given in Appendix II. For multiphoton processes, the steady-state condition is reached when the overall laser pumping rate equals the overall unimolecular reaction rate. In general, for molecules like ethyl acetate the steady-state is reached only for $F_t > 0.80$ and the steady-state contribution to the overall reaction yield is very small (see Appendix II) except at high fluence. In the steady-state or

(9) Jang, J. C. Ph.D. Dissertation, Kansas State University, 1981.

(10) (a) Quack, M. *J. Chem. Phys.* **1979**, *70*, 1069. (b) Quack, M. *Ber. Bunsenges. Phys. Chem.* **1979**, *83*, 757. (c) Quack, M.; Hunbert, P.; Van den Bergh, H. *J. Chem. Phys.* **1980**, *73*, 247.

(11) Black, J. G.; Kolodner, P.; Schulz, M. J.; Yablonovitch, E.; Bloembergen, J. *Phys. Rev. A* **1979**, *19*, 704.

(12) Plum, C. N.; Houston, P. L. *Chem. Phys.* **1980**, *45*, 159.

high-fluence ($F_R > 0.8$) regime, most reaction occurs during the pulse. Since the postpulse reaction is, therefore, negligible, F_R is directly related to the experimental reaction yield, and the steady-state rate constant, $k_1(st)$, can be obtained fro the linear portion of the ln $(1 - F_R)$ vs. ϕ plot. The biparticular rate constant,[10b] $k_1(st) = k_{uni}(st)/I$, is more useful than $k_{uni}(st)$ unless time-resolved experiments are done.

The $k_1(st)$ values do not seem to depend on the intensity (see Appendix II), and experimental plots of ln $(1 - F_R)$ vs. ϕ can be made with data for which time (pulse length) was held constant but intensity varied in order to change fluence. The serious problem of extracting experimental $k_1(st)$ values is the need to accurately measure F_R at very high fractional reaction; the present calculations suggest the limiting slope should be derived from data for which $P(\phi) \geq 0.80$. However, on the positive side, $k_1(st)$ is very sensitive to the cross-section model. On the other hand, $k_1(st)$ is not very sensitive to k_i. When k_i was increased by 10 for all i above E_0, $k_1(st)$ was increased only by 50% for both models a and b. Therefore, within the uncertainty of a factor of 2 in k_i, $k_1(st)$ can directly test the absorption cross-section model and can be an important experimental measurement.

In the intermediate regime (which includes the largest ϕ range), simple kinetic schemes such as evaluating the postpulse reaction from a Boltzmann distribution or application of the steady-state cannot be used and full detail must be considered. In the following paragraphs the dependence of the reaction probability on intensity, fluence and $\langle n \rangle$ will be considered. To examine the intensity dependence in the absence of collisions, three calculations were done. Since neither a bottleneck in the absorption model or collisions are included, the only possible dependence of reaction probability on intensity must arise from different extents of reaction during the pulse. Calculations[9] using model a cross sections with three pulse shapes [(i) a 300-ns rectangular pulse, (ii) a 2-μs rectangular pulse (the intensity was reduced by 3/20 for (ii), and (iii) a 300-ns pulse containing 5-ns spikes every 25 ns (the intensity of the 5-ns spike was five times greater than the 300-ns rectangular pulse)] verified these conclusions. Of special interest was the comparison of results from (i) and (iii) since the latter resembles the experimental laser pulse. The F_R were nearly the same for the 300-ns pulse (without spikes) and the 300-ns pulse (with spikes). The small difference is due to different extent of reaction during the spike; only molecules which have lifetimes less than 25 ns can react during the spike. A 25-ns lifetime corresponds to a vibrational energy of 120 kcal mol^{-1}, and molecules with such energy make a small contribution to F_R. If collisions occur during the pulse, a competition with laser pumping also may arise and may introduce an intensity dependence to the reaction probability.[13-16] Calculations were done for 100- and 300-ns pulses and $\phi = 2$ J cm^{-2} with collisions included for a room-temperature bath gas at 0.05 and 2.0 torr; stepladder collisional transition probabilities with $\langle \Delta E_d \rangle = 6$ kcal mol^{-1} were used for all levels ($P_{ij} = 1.0 - P_{ji}$ for $E_i - E_j = \Delta E_d$; otherwise $P_{ij} = 0$). On the average, one collision will occur every 100 ns at 2 torr, and 0.05-torr collisions are of negligible importance during the 300-ns pulse. Indeed, at 0.05 torr F_R^∞, F_R, and $\langle n \rangle$ were the same as for the collisionless case with the 300- and 100-ns pulses. Although the collision rate at 0.05 torr is not sufficient to affect the energy absorption, collisions still are important for the postpulse processes. At 2.0 torr, F_R^∞ was lowered by 30% for the 300-ns pulse relative to the 100-ns pulse. As the pressure increases, collisional deactivation competes with the infrared pumping process; therefore, F_R^∞ and the vibrational energy distributions becomes dependent on intensity.

We conclude that, for constant ϕ, intensity is unimportant (for our incoherent model) in determining $\langle n \rangle$, F_R, and F_R^∞ except
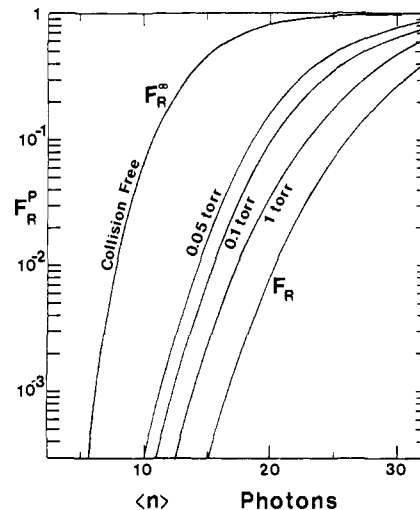

Figure 5. Plot of reaction yields vs. $\langle n \rangle$ for variable pressures of a cold bath gas. The reaction yield, F_R^P, is F_R + postpulse reaction (collisional deactivation). Calculations are done for a 300-ns pulse with collisional transition probabilities given by a stepladder model with $\langle \Delta E_d \rangle = 2100$ cm^{-1} (6 kcal mol^{-1}). Collisions during the pulse were included in the calculation, but the transition probabilities were set to zero for levels below 35 kcal mol^{-1}.

for high ϕ in which reaction during the pulse competes with laser pumping or for pressures sufficiently high that collisions during the pulse compete with laser pumping. Therefore, a Gaussian-shaped pulse (the experimental situation) will give the same results as the rectangular pulse (the model calculations). Indeed, calculations[9] with a Gaussian pulse gave identical results.

Plots[9] of F_R^∞ vs. ϕ show a strong dependence on cross-section model. This dependence is largely a consequence of the different $\langle n \rangle$ at the same ϕ, and, as shown in Figure 3, F_R^∞ vs. $\langle n \rangle$ is not so dependent on model. The slopes of the log F_R^∞ vs. log ϕ plots are 6-8 for the lower ϕ range, which agrees with the experimental results.[1] Since F_R^∞ is so highly dependent on ϕ, (for example, a 20% change in ϕ at 0.5 J cm^{-2} changes F_R^∞ by a factor of 5), very accurate ϕ measurements are necessary to obtain experimental data that are suitable for matching to model calculations. At higher ϕ this problem is less severe because of the lower order dependence of F_R^∞ on ϕ. Although the F_R^∞ vs. $\langle n \rangle$ plots also are very dependent on the ϕ measurements, such plots are preferred because comparisons, at least, are being made for the same absorbed energy.

The calculated F_R and F_R^∞ values in this section should not be directly compared to experimental yields in bulb experiments because *very important* post-pulse collisional phenomena are not included. Such collisional effects are discussed next and in section IV when attempts are made to match calculated and experimental reaction probabilities for ethyl acetate and ethyl fluoroacetate.

4. Postpulse Considerations. The calculations in Section III 3 showed that the energy distributions for moderate $\langle n \rangle$ were close to Boltzmann and a large fraction of molecules were above E_0. Therefore, for large molecules with rather low k_i values, postpulse collisional relaxation and bulk cooling processes must be considered. The cooling processes are especially important for irradiation of pure reagent since molecular $V-T,R$ relaxation in the irradiated volume cannot quench the reaction; i.e., the energy *must* be removed from the irradiated volume by bulk cooling processes in order to prevent the ester dissociation reaction from continuing by thermal activation. The discussion will be in two parts: (i) irradiation of samples with excess inert gas and (ii) irradiation of pure reagent samples (according to our model, all molecules absorb the laser energy).

First, consider case i with excess inert gas deactivating the reactant molecules without a change in the temperature of the sample. In principle, the postpulse reaction yield can be calculated simply from the competition between unimolecular reaction and collisional deactivation.[6] The calculated reaction probability, F_R^P,

(13) Jang, J. C.; Setser, D. W. *J. Phys. Chem.* **1979**, *83*, 2809.

(14) Bado, P.; Van den Berg, H. *J. Chem. Phys.* **1978**, *68*, 4188.

(15) (a) Stone, J.; Thiele, E.; Goodman, M.; Stephenson, J. C.; King, D. S. *J. Chem. Phys.* **1980**, *73*, 2259. (b) Stephenson, J. C.; King, D. S.; Goodman, M. F.; Stone, J. *Ibid.* **1979**, *70*, 4496.

(16) (a) Quick, C. R., Jr.; Wittig, C. *Chem. Phys.* **1978**, *32*, 75. (b) Quick, C. R., Jr., Wittig, C. *J. Chem. Phys.* **1978**, *69*, 4201.

which is F_R plus the postpulse reaction yield, is plotted in Figure 5 for various pressures of bath gas for a stepladder model with $\langle \Delta E_d \rangle = 6$ kcal mol^{-1}. Plots of other $\langle \Delta E_d \rangle$ are presented in section V for ethyl fluoroacetate. In this calculation, the stepladder deactivation model was applied to levels ≥ 35 kcal mol^{-1}, which is ~10 kcal mol^{-1} below E_0. Except for the 1 torr case where this eliminates collisional effects on the absorption process, this restriction has no influence on the generality of the results. Collisions dramatically reduce the yield from the collision-free result with the extent of reduction increasing with pressure, $\langle \Delta E_d \rangle$, and decreasing $\langle n \rangle$. For high fluence the collisional effects are less important because a higher fraction of reaction occurs during the pulse.

A Stern–Volmer plot for quenching of ethyl acetate by a bath gas for fixed fluence; i.e., a plot of $(F_R{}^P)_0 / F_R{}^P$ vs. pressure of bath gas, where $(F_R{}^P)_0$ is the yield in the absence of bath gas, was shown in the preceding paper.[1] Both the experimental data and the calculations show that the deactivation efficiency is highly dependent on ϕ (or $\langle n \rangle$). As will become apparent in the next paragraph, obtaining $(F_R{}^P)_0$ by calculations for bulb experiments is *very* difficult. Therefore, the Stern–Volmer-type presentation is not the best way to compare data and model calculations. A better way is to compare calculated and experimental results via plots of $P(\langle n \rangle)$ vs. $\langle n \rangle$ for constant pressure of bath gas. This is done for $FCH_2COOC_2H_5$ in CF_4 and He bath gases in section IV.

Consider next irradiation of the pure reagent gas. According to the model, all molecules in the irradiated volume become vibrationally excited with distributions resembling those shown in Figure 4. The first relaxation step will be collisions of vibrationally excited molecules in the irradiated volume with themselves, which leads to equilibration with Boltzmann temperature T'.

$$\langle E_{vib} \rangle + \langle E_{rot} \rangle_{300 \text{ K}} + \langle E_{trans} \rangle_{300 \text{ K}} \rightarrow$$
$$\langle E_{vib} \rangle_{T'} + \langle E_{rot} \rangle_{T'} + \langle E_{trans} \rangle_{T'} \quad (6)$$

The left-side terms are the energies upon termination of the laser pulse; the right-side terms are energies after equilibration within the irradiated volume. Starting with $\langle E_{vib} \rangle = 38$ kcal mol^{-1} for ethyl acetate, T' is 1075 K and $\langle E_{vib} \rangle - \langle E_{vib} \rangle_{T'} = 6.4$ kcal mol^{-1}. This demonstrates that the relatively small translational and rotational heat capacity does not provide a significant energy sink for large polyatomic molecules; therefore, a *thermal* unimolecular reaction may continue within the irradiated volume after the $V-T,R$ energy equilibration step, especially for exoergic or midly endoergic reactions. The thermal reaction will continue with rate constant $k(T')$ until the T' of the irradiated volume is lowered by bulk cooling processes.

The final relaxation step is energy flow from the irradiated volume to the surrounding cold gas sheath. The combination of molecular flow, bulk diffusion, thermal conduction, bulk expansion, and shock expansion will be identified collectively as a "cooling wave". The cooling time will depend on pressure, deposited energy, and the geometry of the irradiated volume. Experiments with the thermal monitor in the preceding paper[1] showed that the "cooling wave" is sufficiently rapid at 0.05 torr to quench the "thermal" reaction *of the monitor molecule*. Using the absorbed energy to calculate T', the Arrhenium expression to calculate $k(T')$ and the estimated extent of thermal reaction from the thermal monitor experiments for A/A_0 gives an estimate $(A/A_0 = \exp(-k_\infty(T')\Delta t))$ of Δt. This corresponds to $\Delta t \leq 5$ μs at 0.05 torr based on the virtual absence of reaction by the thermal monitor at $\langle n \rangle = 20$. The fraction of molecules that would diffuse out of the irradiated volume was calculated[9] for a beam radius of 0.85 cm for several temperatures as a function of time. Half of the molecules diffused outside the irradiated volume after 55, 35, 26, and 20 μs at 800, 1000, 1200, and 1400 K, respectively. According to the thermal monitor experiments, the cooling process is faster than diffusion and shock expansion may be the main cooling process. All of the cooling processes are expected to be T' dependent and the cooling time will become shorter with increasing T' (or $\langle n \rangle$). Although detailed modeling of the cooling wave has not been presented, other authors[17,18] also have come to the conclusions that the time scale

is 5–10 μs for the irradiation geometries of our experiments.[1]

In summary, the total reaction yield for irradiation of a neat sample is the sum of the reaction during the laser pulse, reaction before equilibration, and the thermal reaction after equilibration. If only some fraction of the molecules is excited by the laser, then $V-V$ transfer must be included with $V-TR$ equilibration. This complicates modeling the equilibration step; however, the same T' still will be developed and a cooling wave is still essential to quench the thermal reaction. An alternative formulation is simply to define some "effective deactivation (or cooling) rate" and allow this to compete with chemical reaction from each energy region of the distribution.[11] The postpulse reaction for ethyl acetate and ethyl fluoroacetate is discussed further in section IV; the *relative* contribution of the postpulse reaction to the total reaction probability is higher at low ϕ, even though the absolute postpulse reaction yield is lower.

IV. Reaction Probability for Ethyl Acetate and Ethyl Fluoroacetate

1. Computation of $P(\langle n \rangle)$ for Ethyl Acetate. The reaction probability for irradiation of 0.05 torr of ethyl acetate with the P_{38} and P_{20} lines was calculated in two steps. First, the reaction yield during the pulse was computed from eq 1. Then estimates were made for the postpulse contribution to reaction. In fitting the variation of $\sigma_L(\phi)$, $P(\phi)$, or $P(\langle n \rangle)$, the experimental uncertainty should be kept in perspective. In our experiments[1] $\sigma_L(\phi)$ was determined from the transmittance, $\ln (\phi/\phi_0)$; a ±1% error in the transmittance gives ±10% error in $\sigma_L(\phi)$. Errors in σ_L and ϕ both appear in $\langle n \rangle$, because $\langle n \rangle = \phi_0 \sigma_L(\phi)$ and a ±5% uncertainty ϕ_0 is normal. The expected uncertainty for $\langle n \rangle$ is then ±15%. Since the reaction probability is a strong function of $\langle n \rangle$, this uncertainty introduces a significant uncertainty in the experimental $P(\langle n \rangle)$ values. An additional uncertainty in $P(\phi)$ is the determination of the irradiation volume. The expected experimental uncertainties are indicated in the figures where calculations are compared with experimental results.

Equation 1 was integrated for a realistic laser pulse shape (a sum of two Gaussian distributions, one (40%) centered at 100 ns and the other (60%) at 500 ns) with an energy level spacing of 3 kcal mol^{-1}. The RRKM k_i values were calculated as discussed in Appendix I. The $\sigma_{i+1,i}$ were chosen so that the calculated $\sigma_L(\phi)$ values matched the experimental $\sigma_L(\phi)$ values. A stepladder collisional deactivation model with $\langle \Delta E_d \rangle = 6$ kcal mol^{-1} was employed for levels above 35 kcal mol^{-1}: i.e., $P_{ij} = 0$ for $E_i - E_j \neq 6$ kcal mol^{-1} and $E_j \leq 35$ kcal mol^{-1}; $P_{ij} = 1.0 - P_{ji}$ for $E_i - E_j = 6$ kcal mol^{-1}. However, at 0.05 torr $\omega = 4.7 \times 10^5$ s^{-1} and collisions have negligible importance during the laser pulse. Three different empirical $\sigma_{i+1,i}$ models (Figure 6) with the stimulated emission cross section fixed by detailed balance were used for the P_{20} and P_{38} frequencies and the calculated $\sigma_L(\phi)$ values are shown in Figure 7. Below $F_R < 0.05$ (i.e., $\phi \leq 2$ J cm^{-2}) reaction during the pulse is insignificant and the $\sigma_L(\phi)$ values reflect the energy dependence of the net microscopic cross sections. The model I cross sections, $\sigma_{i+1,i} = \sigma_{10}$ for P_{20} and $\sigma_{i+1,i} = \sigma_{10}((i^{1/5} \times 8) - 7)$ for P_{38}, give satisfactory (±15%) match with the experimental data. Since $\sigma_L(\phi)$ for P_{20} irradiation does not increase with ϕ, models II and III, which were investigated as a possible way to minimize F_R for the same $\langle n \rangle$, are unacceptable. For P_{38} models II and III are not as good as for I but they probably are within the experimental uncertainty. The calculated F_R and $F_R{}^\infty$ for the P_{20} and P_{38} lines are presented in Figure 8. As expected from the model calculations, the rather small differences in models I, II, and III had little effect on the calculated F_R for either P_{20} or P_{38}. However, the rather *extreme difference* between the P_{38} and P_{20} cross-section models do give significantly different F_R, and even $F_R{}^\infty$, for the same $\langle n \rangle$. This difference in F_R is roughly an order of magnitude and correlates with the much higher exper-

(17) Steel, C.; Starov, V.; Leo, R.; John, P.; Harrison, R. C. *Chem. Phys. Lett.* **1979**, *62*, 121.

(18) Smith, G. P.; Laine, R. M. *J. Am. Chem. Soc.*, in press.

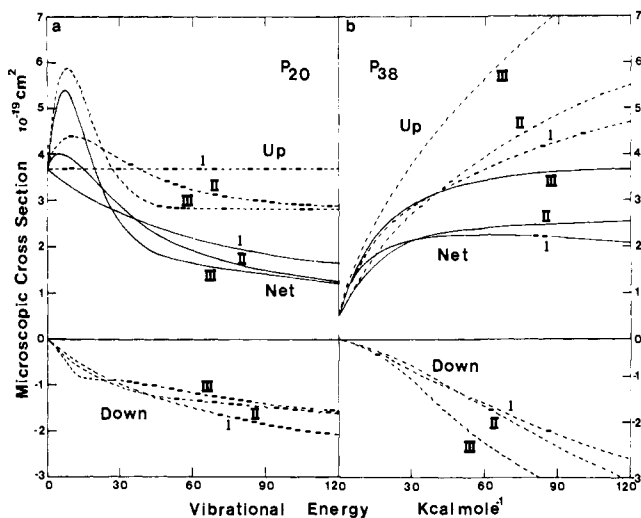(19) Luu, S. H.; Troe, J. *Ber. Bunsenges. Phys. Chem.* **1974**, *78*, 766.

Figure 6. Microsopic absorption cross-section models for irradiation of ethyl acetate with the P_{20} and P_{38} laser frequencies. Upper dashed curves are up-transition and lower dashed curves are down-transition cross sections. Solid curves are the net absorption cross sections, $\sigma_i' = \sigma_{i+1,i} - \sigma_{i-1,i}$. The models are defined by the $\sigma_{i+1,i}$ values, which are empirical in nature. For both frequencies model I provides the best fit to the $\sigma_L(\phi)$ data. The P_{20} and P_{38} model I cross sections are given by $\sigma_{i+1,i} = \sigma_{10}$ and $\sigma_{i+1,i} = \sigma_{10} (8 \times i^{1/5} - 7)$, with $\sigma_{10} = 3.7 \times 10^{-19}$ cm², respectively.
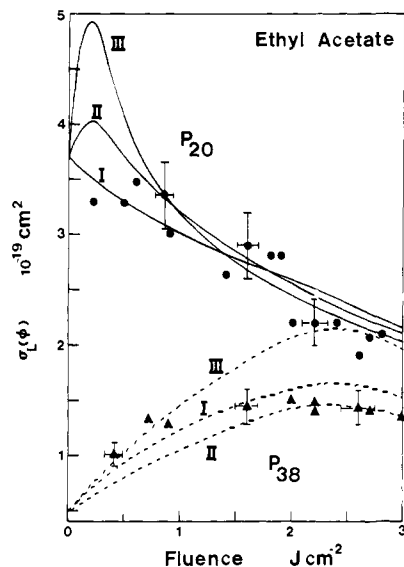

Figure 7. Comparison of the calculated and experimental $\sigma_L(\phi)$ for the three microscopic cross-section models. Typical uncertainties are indicated on some points by the error bars. Model I, for both P_{38} and P_{20}, gives the best fits to the experimental data. The calculations are for a 1-μs Gaussian-shaped pulse (see text) with collisions included during the laser pulse.

imental[1] reaction probability for P_{38} than for P_{20}, even for the same $\langle n \rangle$. The rapid increase with energy of the P_{38} microscopic net cross sections (five to seven times higher than σ_{10}) gives a broader vibrational distribution than for the P_{20} models.

If F_R is > 0.5, postpulse reaction is not important; however, for $F_R \lesssim 0.2$ the postpulse contribution must be included. According to our previous treatment, the postpulse reaction can be divided into two components: (i) the reaction that occurs during the energy equilibration period (this requires ca. one to three collisions, and we will allow 3 μs for this period at 0.05 torr) and (ii) the reaction that occurs after equilibration but before the "cooling wave" quenches the thermal reaction. The reaction during the equilibration time was taken as

$$F(3\ \mu s) = \sum_{i > E_0} \frac{k_i}{k_i + (3\ \mu s)^{-1}} N_i(t_p)$$
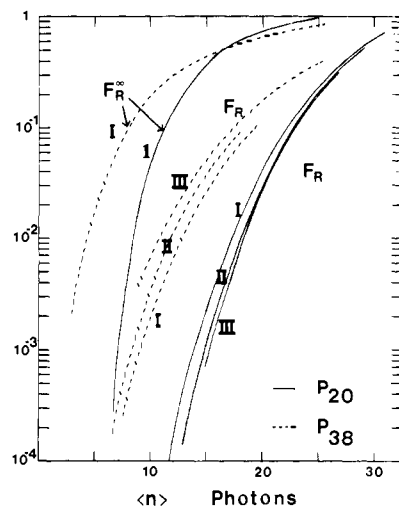
Figure 8. Plot of calculated F_R and F_R^∞ of ethyl acetate vs. $\langle n \rangle$ for the three cross-section models given in Figure 6; solid lines are for P_{20} and dashed lines are for P_{38}.
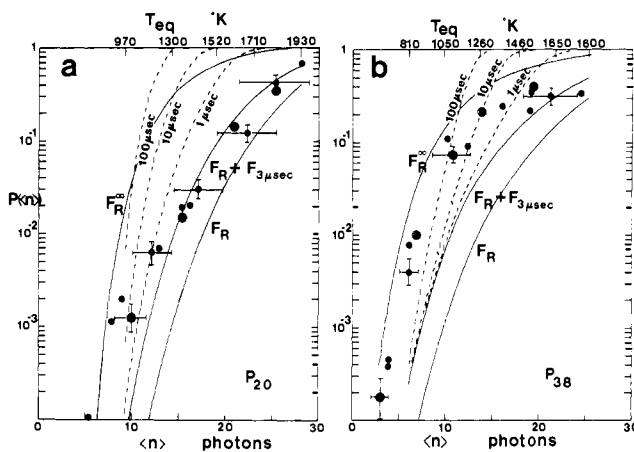

Figure 9. Comparison of calculated and experimental $P(\langle n \rangle)$ vs. $\langle n \rangle$ for ethyl acetate. (a) Plot of F_R, F_R^∞, $F_R + F(3\ \mu s)$ and $F_R + F(3\ \mu s) + F_T(t)$ vs. $\langle n \rangle$ for model I cross sections (of Figure 6) for P_{20} irradiation of ethyl acetate. For the definitions of $F(3\ \mu s)$ and $F_T(t)$, see text. The dotted lines are $F_R + F(3\ \mu s) + F_T(t)$. The equilibrium temperatures, T, are indicated in upper scale for several $\langle n \rangle$. The error bars on a few of the experimental points indicate the expected experimental uncertainty. (b) Same plot as (a) but for P_{38} excitation of ethyl acetate; calculations are for model I cross sections of Figure 6. Double circled entries are experimental points selected so that reaction probability for P_{20} and P_{38} were measured at the same absorbed energy.

where $N_i(t_p)$ is the vibrational distribution at the termination of the laser pulse.

Based upon the diffusion time calculation,[9] the time for the cooling wave would be ~25 μs for $\langle n \rangle$ = 15 and ~50 μs for $\langle n \rangle$ = 7. However, processes such as shock and thermal expansion may be more rapid. The thermal monitor experiments suggest that cooling times (after the 3 μs equilibration time) of 1–10 μs are reasonable for $7 \lesssim \langle n \rangle \lesssim 15$. The thermal reaction component, $F_T(t)$, was calculated from *the thermal rate constant* for $t = 1$, 10, and 100 μs; T' was obtained from $\langle n \rangle$ and eq 6. The total calculated reaction probability, $F_R + F(3\ \mu s) + F_T(t)$ is presented in Figure 9; the collisionless yield, F_R^∞, is shown for reference. For P_{20}, including $F(3\ \mu s)$ increases the yield by a factor of ~10 at $\langle n \rangle$ = 12, and allowing 1 μs for cooling adds another factor of 5.

The calculated and experimental yields compare favorably for excitation with the P_{20} line (Figure 9a) providing that a progressively longer cooling period is allowed for lower $\langle n \rangle$ experiments. The situation, however, is not so pleasing for excitation of ethyl acetate with the P_{38} line (Figure 9b) since the calculations *underestimate* the experimental reaction probability. The ratio
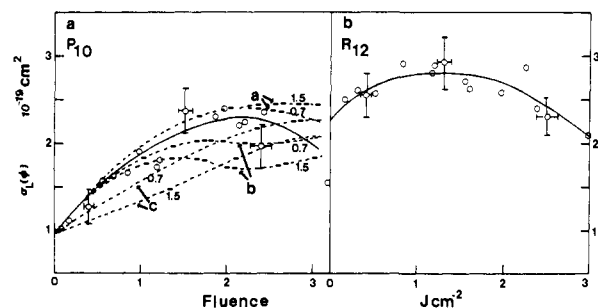
Figure 10. Comparison of calculated and experimental $\sigma_L(\phi)$ for P_{10} and P_{12} excitation of ethyl fluoroacetate. The microscopic cross-section models used in these calculations are $\sigma_{i+1,i} = \sigma_{10}(0.3\sqrt{i} + 0.7)$ and $\sigma_{i+1,i} = \sigma_{10}(1.2\sqrt{i} - 0.2)$ for $_{12}$ and P_{10} excitation, respectively. Stimulated emission from detailed balance were also included. The experimental $\sigma_L(\phi)$ values for pure ethyl fluoroacetate are given by open circles. The dotted curves are calculated results corresponding to the CF_4 experiments for different collision models: (a) stepladder model with $\langle \Delta E_d \rangle = 3$ kcal mol^{-1} for levels with $E \geq 35$ kcal mol^{-1} and $P_{ij} = 0$ for all levels below 35 kcal mol^{-1}; (b) the same as for (a) but $\langle \Delta E_d \rangle = 6$ kcal mol^{-1}; (c) the same as (a) but all levels were fit to $\langle \Delta E_d \rangle = 3$ kcal mol^{-1} stepladder model. The number on the calculated curves are the CF_4 pressures.

of $F_R(P_{38})/F_R(P_{20})$ is 45, 11, 5, and 2 at $\langle n \rangle = 12$, 15, 18, and 22, which is the correct trend to fit the data. Adding $F(3\ \mu s)$ has about the same effect for both calculations. The thermal reaction component will be identical for the same $\langle n \rangle$ since this gives the same T', and the apparently smaller thermal contribution to the P_{38} data is a consequence of the higher F_R (see Figure 9). Even long thermal reaction times are inadequate to match $P(\langle n \rangle)$ for $\langle n \rangle \leq 15$ for P_{38} excitation. The long cooling times not only are physically unrealistic but, in fact, are ruled out by the thermal monitor experiments.[1] We must conclude that our formulation is inadequate to explain the P_{38} data. No set of microscopic cross sections can simultaneously match the $\sigma_L(\phi)$ values and the observed reaction probabilities for P_{38} irradiation.

Why does the model work for P_{20} irradiation but not for P_{38} irradiation? The substantial differences in P_{38} and P_{20} microscopic cross sections do partially explain the different reaction probabilities, but additional factors must be considered. We believe that a low-energy, intensity-dependent bottleneck exists for absorption of P_{38} photons for a certain fraction of the molecules. This bottleneck prevents some molecules from absorbing photons and results in a bimodal (or multimodal) vibrational energy distribution. Thus, for the same $\langle n \rangle$ the *excited* molecules from P_{38} irradiation have much higher energy than for P_{20} irradiation. Experimental support for this explanation is provided by the limiting high fluence reaction probability for P_{38} excitation, which appears to be ~ 0.5 rather than 1.0.

2. Computations of $P(\langle n \rangle)$ for Ethyl Fluoroacetate. The calculations described for ethyl acetate also were performed for ethyl fluoroacetate for irradiation by the P_{10} and R_{12} frequencies. The RRKM rate constants were calculated using the same models as for ethyl acetate except that frequencies were changed to account for substitution of a H atom by a F atom and E_0 was lowered to 46.0 kcal mol^{-1}. Microscopic cross sections that monotonically increase with vibrational energy reproduce the dependence of $\sigma_L(\phi)$ on fluence. The $\sigma_L(\phi)$ increase with ϕ for both frequencies before declining because reaction during the pulse becomes appreciable (see Figure 10).

The reaction probabilities, including allowance for postpulse reaction, are compared with the data in Figure 11. The R_{12} data resemble the results for the P_{20} excitation of ethyl acetate, whereas the P_{10} data of $CH_2FCOOC_2H_5$ fall between the P_{20} and P_{38} excitation of ethyl acetate. Nevertheless, $P(\langle n \rangle)$ differs at the same $\langle n \rangle$ for the two sets of $CH_2FCOOC_2H_5$ data. The agreement between the experimental $P(\langle n \rangle)$ and $F_R + F(3\ \mu s) + F_T(t)$ for R_{12} irradiation is excellent for reasonable choices of t. The limiting $P(\langle n \rangle)$ may be ~ 0.7 rather than unity for R_{12} irradiation, but this is not definitely established. The agreement between the P_{10} irradiation data and the calculated reaction probabilities is good for $P(\langle n \rangle) \gtrsim 0.1$. Below $P(\langle n \rangle) \sim 0.05$, the cooling times
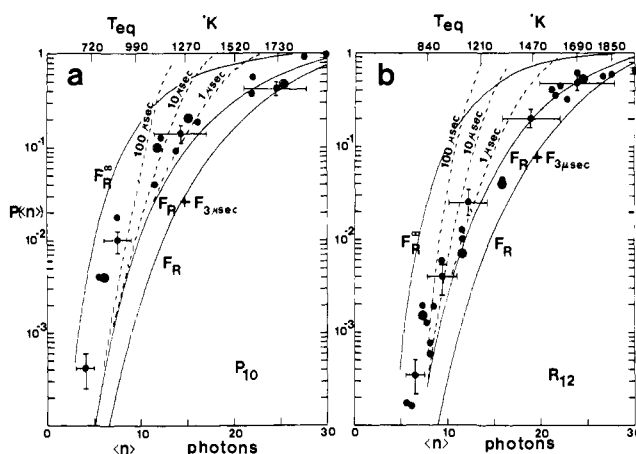

Figure 11. Comparison of calculated and experimental $P(\langle n \rangle)$ of $CH_2FCOOC_2H_5$: (a) for R_{12} excitation, (b) for P_{10} excitation. F_R, F_R^∞, $F_R + F(3\ \mu s)$, and $F_R + F(3\ \mu s) + F_T(t)$ are plotted vs. $\langle n \rangle$; dashed curves are $F_R + F(3\ \mu s) + F_T(t)$. Calculations are for the cross-section model which gave $\sigma_L(\phi)$ shown in Figure 10. Double circles in these figures are the new experimental points selected so that the reaction probabilities were measured at the same absorbed energies. Upper scale is the thermal equilibrium temperature, T.
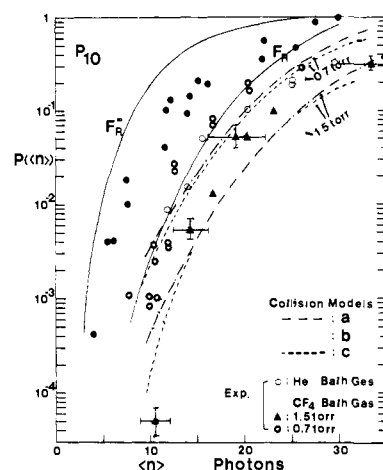

Figure 12. Comparison of calculated and experimental $P(\langle n \rangle)$ in the presence of inert bath gases for P_{10} excitation of $CH_2FCOOC_2H_5$: (●) experimental points for 0.05 torr of ethyl fluoroacetate, (▲) 1.5 and (○) 0.7 torr of added CF_4, (○) 3.5 torr of added He. The different calculated results with CF_4 bath gas are for collisional deactivation model a, $-\cdot-$, model (b), ..., and model c $---$, which are defined in the caption of Figure 10. The upper set of curves is for 0.7 torr and the lower set is for 1.5 torr of CF_4.

required to match the data are unreasonable and the model cannot describe the reaction yield data. In contrast to the P_{38} $CH_3COOC_2H_5$ data the P_{10} $CH_2FCOOC_2H_5$ reaction probabilities do approach unity at high ϕ. Although it may be a coincidence, the longer wavelength excitation for both $CH_3COOC_2H_5$ and CH_2-$FCOOC_2H_5$ are the cases for which the experimental $P(\langle n \rangle)$ values are higher than the calculated values. In both instances the increased reaction probability can be rationalized by fluence-dependent rotational fractionation; i.e., only a certain fluence-dependent fraction of molecules at 300 K are in rotational levels which are in resonance with the laser pump frequency.

3. $P(\langle n \rangle)$ for $CH_2FCOOC_2H_5$ in CF_4 and He. The reaction probability of $CH_2FCOOC_2H_5$ was measured for P_{10} irradiation with variable fluence but constant pressure of CF_4 (0.7 torr, 1:15 mixture and 1.5 torr, 1:30 mixture) and He (3.5 torr, 1:70 mixture). The reaction probabilities are shown in Figure 12. Measurements of $\sigma_L(\phi)$ with 1.5 torr of CF_4 showed that the energy absorption was the same as for neat samples; therefore, the same $\sigma_{i+1,i}$ were used for these calculations.

Stepladder models with $\langle \Delta E_d \rangle = 3$ (model a) and 6 (model b) kcal mol^{-1} were selected[6b,19] for levels above 35 kcal mol^{-1} for

the collision with CF_4. Collisions were ignored for levels below 35 kcal mol^{-1}. This certainly is incorrect at 1.5 torr of CF_4 since the collision frequency is 1.6×10^7 s^{-1} $torr^{-1}$ and collisional processes will interact with the energy absorption processes. In order to examine the effect of deactivating collisional transitions for lower levels, calculations were done for the 1:15 and 1:30 mixtures, using the stepladder model for all levels with $\langle \Delta E_d \rangle = 3$ kcal mol^{-1} (model c in Figure 12). Although models a and c give similar reaction yields at the same absorbed energy (see Figure 12), the model with deactivating collisions for all levels gives $\sigma_L(\phi)$ which is lower than for the pure gas (see Figure 10). For model c, collisions during the laser pulse result in deactivation, and this completes with up-pumping by laser absorption. The ethyl fluoroacetate microscopic cross sections increase with vibrational energy, and collisional deactivation during the laser pulse lowers the average energy. The experimental absorption measurements with up to 2 torr of CF_4 show that $\sigma_L(\phi)$, in fact, is unchanged. Thus, excluding collisional deactivation for the low levels provides a better match to the absorption data for the 0.7 and 1.5 torr of CF_4 experiments.

The $\langle \Delta E_d \rangle = 3$ and 6 kcal mol^{-1} calculations are presented in Figure 12; the reaction yields are very dependent on pressure. The $\langle \Delta E_d \rangle = 3$ kcal mol^{-1} curves match the reaction yield data for both sets of CF_4 data. Because of the lack of knowledge about the lower level collisional transition probabilities and low-energy bottleneck effects, our treatment may not be appropriate at low ϕ. With benefit of hindsight, the best way to eliminate complications due to collisions in the lower levels is to do inert bath gas experiments with a sufficiently short laser pulse so that collisions during the pulse are negligible, but with sufficiently high pressures that collisional deactivation dominates the postpulse processes. An important point is the better *general* agreement of the *calculations with bath gas* as opposed to those without bath gas in the low ϕ region. This is convincing evidence that simple competition between deactivation and reaction is a realistic treatment for the postpulse processes. Carefully designed inert gas experiments may be the simplest way to do quantitative studies of multiphoton laser-induced reactions of large molecules which have very complicated postpulse kinetic effects for neat samples.

Experimental reaction probabilities of ethyl fluoroacetate with He as a bath gas are also presented in Figure 12. The results show that 3.5 torr of He gives less quenching than 1.5 torr of CF_4; this is a normal trend for deactivation of highly vibrationally excited molecules.[6] Model calculations for the He data were not done because a less efficient collision model (exponential model) requires a finer grain size (~ 1 kcal mol^{-1}), and the calculations became very expensive.

V. Discussion

1. Characteristics of the Rate Equation Model. The master equation formulation assumes incoherent energy absorption, rapid internal energy relaxation, and statistical rate constants, which is Quack's limiting case B.[20] Stone and Goodman[21] have showed that the critical requirement for incoherent pumping is that the dephasing frequency be larger than the Rabi frequency, ω_R. This criterion is satisfied in the quasi-continuum energy region[15,21,22] where numerous independent experiments have demonstrated the existence of strong interactions,[23-25] even though these interactions may not be well understood. An obvious question is: why does the rate equation formulation seem to fit the ethyl acetate and
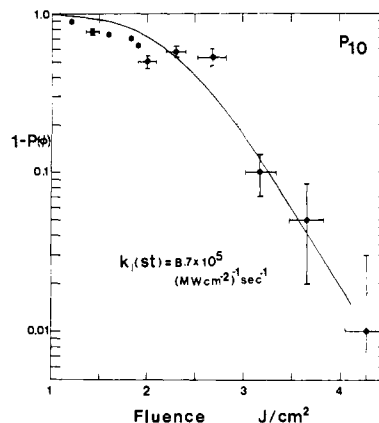
(20) Quack, M. *J. Chem. Phys.* **1978**, *69*, 1282.

(21) (a) Stone, J.; Goodman, M. F. *J. Chem. Phys.* **1979**, *71*, 408. (b) Stone, J.; Thiele, E.; Goodman, M. F. *Chem. Phys. Lett.* **1980**, *71*, 171.

(22) Galbraith, H.; Ackerhalt, J. "Laser Induced Chemical Processes"; Steinfeld, J. I., Ed.; Plenum: New York, 1981; Vol. I.

(23) (a) Ko, A. N.; Rabinovitch, B. S. *Chem. Phys.* **1978**, *29*, 271; **1978**, *30*, 361. (b) Walters, F. C.; Rabinovitch, B. S.; Ko, A. N. *Ibid.* **1980**, *49*, 65.

(24) (a) Beck, S. M.; Powers, D. E.; Hopkins, I. B.; Smalley, R. E. *J. Chem. Phys.* **1980**, *73*, 2019. (b) Hopkins, J. B.; Powers, D. E.; Smalley, R. E. *Ibid.* **1980**, *73*, 683.

(25) Moss, M. G.; Ensminger, M. D.; Stewart, G. M.; Mordaunt, D.; McDonald, J. D. *J. Chem. Phys.* **1980**, *73*, 1257.

Figure 13. Comparison of $\ln (1 - P(\phi))$ vs. ϕ for calculated and experimental results for P_{10} irradiation of ethyl fluoroacetate. In the calculations $F_R(\phi)$ was set equal to $P(\phi)$. Note that steady-state, i.e., linear plot, is achieved only at $P(\phi) \gtrsim 0.70$. $k_1(st) = 8.7 \times 10^5$ $(MW/cm^2)^{-1}$ s^{-1}.

ethyl fluoroacetate data in the $P(\langle n \rangle) \geq 10^{-2}$ range, even though the density of vibrational states following absorption of one or two photons is inadequate to qualify for a true quasi-contunuum? This question, as well as the question of how such a large fraction of molecules can absorb laser radiation and react, is addressed in the next section which deals with the spectroscopic properties of ethyl acetate. Matching the calculated and experimental $\sigma_L(\phi)$ was a very important part of our investigation, and numerical calculations (as opposed to analytic calculations for simpler $\sigma_{i+1,i}$ models) for fully variable sets of $\sigma_{i+1,i}$ seemed the best way to reach our objective. In our calculations the energy dependence of $\sigma_{i+1,i}$ is entirely responsible for the ϕ dependence of $\sigma_L(\phi)$, except for the decline when unimolecular reaction during the laser pulse becomes appreciable. The $\sigma_{i+1,i}$ values deduced from matching the $\sigma_L(\phi)$ values are phenomenological parameters.

The high density of rotational states explains why the $\sigma_L(\phi)$ values match the broad-band spectroscopic cross sections at $\phi \leq 0.1$ J cm^{-2}. Even for incoherent excitation, the $\sigma_{i+1,i}$ values can have wavelength and energy dependence because of the different oscillator strengths of the states grouped into a given level. Any reinterpretation of our net cross sections in terms of more physical models should recognize that we used the total density of vibrational states in the detailed balance relationship defining stimulated emission. In principle, the energy dependence of $\sigma_{i+1,i}$ could be discussed in terms of more fundamental models developed by Stone, Goodman, and co-workers[15,21] or by Galbraith and Ackerhalt.[22] Both groups have shown that the number of states that interact with the pump mode in the quasi-continuum must be reduced relative to the total density of states to prevent absorption cross sections from declining to vanishingly small values. In fact, our $\sigma_{i+1,i}$ values[26,27] decline very little or even increase with increasing energy. Moreover, the ϕ dependence of $\sigma_L(\phi)$ does not change from methyl acetate to butyl acetate[1] even though the density of states increases much more rapidly for the larger molecules. Either the interacting states are greatly limited or the fundamental assumptions in the theories need modification.

Based upon the variation of calculated reaction probability with time (or $\langle n \rangle$), the threshold, intermediate, and steady-state regimes were qualitatively identified. In the threshold regime, the molecules may be pumped to relatively high vibrational energy (for large molecules the mean energy actually may be $\geq E_0$), but the unimolecular rate constants still are sufficiently small that little reaction occurs during the pulse. In the threshold regime, postpulse reaction makes the most important contribution to the reaction yield. In the intermediate regime, reaction during the pulse and postpulse reaction both contribute. An important result not related

(26) Ferrero, J. C.; Jang, J. C.; Setser, D. W. *J. Chem. Phys.*, to be submitted for publication.

(27) Danen, W. C.; Nguyen, H. H.; Setser, D. W. *J. Am. Chem. Soc.* to be submitted for publication.
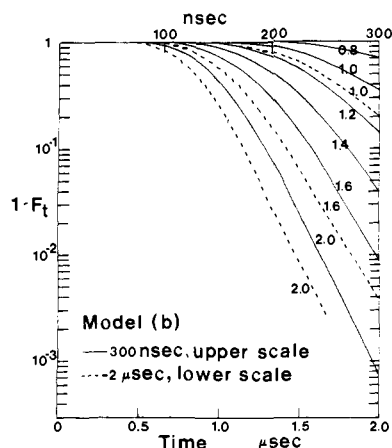
Laser-Induced Chemistry of Organic Esters

J. Am. Chem. Soc., Vol. 104, No. 20, 1982 5449

Figure 14. Plot of $1 - F_t$ vs. time for the fluences (J cm^{-2}) indicated by the numbers in the figure for cross-section model b where F_t is the fraction of reaction at time t. The calculations are for collisionless conditions with a 300-ns (—) and 2-μs ($\cdots$) rectangular pulse. Upper time scale is for the 300-ns case and lower time scale is for the 2-μs case.

to the multiphoton energy deposition is necessity for a postpulse cooling process to quench the thermal reaction that will be driven by the high temperature following V–TR relaxation. In the high-ϕ or steady-state regime most of the reaction occurs during the pulse. A plot of ln $(1 - P(\phi))$ vs. ϕ for the P_{10} excitation of CH$_2$FCO-OC$_2$H$_5$ was examined to search for the steady-state result (see Figure 13 and Appendix II). Only for $P(\phi) > 0.7 \sim 0.8$ is the steady state obtained; however, the experimental plot does have the proper form and seems to give a reasonable steady-state rate constant. Because of the changing intensity of the laser pulse, $k_{uni}(st)$ cannot be obtained simply; however, $k_f(st)$ can be obtained from the linear portion of Figure 13. The steady-state result is a direct test of the pumping model because postpulse contribution to $P(\phi)$ is negligible. The agreement of the experimental points above $P(\phi) = 0.7$ with the model calculations is virtually perfect. This is certainly, in part, fortuitous because of the large experimental uncertainty. Nevertheless, the agreement provides support for a master equation formulation to describe the high fluence condition. Since the $P(\phi)$ data for R$_{12}$ irradiation of CH$_2$FCO-OC$_2$H$_5$ do not go to unity, some adjustment must be made. If $(0.7 - P(\phi))$ is compared[9] with the calculated $1.0 - P(\phi)$ values, moderately good agreement is again found with calculated results.

The calculated reaction yield plus the postpulse contribution matched the experimental reaction probability for P_{20} and R$_{12}$ irradiation of ethyl acetate, and ethyl fluoroacetate, respectively, and for P_{10} irradiation of ethyl fluoroacetate for $P(\langle n \rangle) \gtrsim 0.05$. For P_{38} irradiation of ethyl acetate the calculated $P(\langle n \rangle)$ were lower than the experimental values at all ϕ. Although treatment of the postpulse contribution to reaction is only approximate, the general failure of the model for the P_{38} experiments and for the low $P(\langle n \rangle)$ experiments at P_{10} is attributed to the inability of a certain fraction of molecules to participate in the multiphoton absorption process and was tentatively associated with rotational fractionation in the first absorption step. We find no evidence in the dependence of $\sigma_{i+1,i}$ on energy to suggest vibrational anharmonic bottlenecking. The spectroscopy of ethyl acetate is examined in the next section in order to consider the rotational fractionation and absence of anharmonic bottlenecking.

2. Spectroscopic Considerations of Ethyl Acetate. The 1050-cm^{-1} band is thought to consist of two modes,[28] a C–CH$_3$ stretch plus a C–CH$_3$ rock. The integrated absorption coefficient is 0.2 D, which gives a Rabi frequency, ω_R, of 0.09 cm^{-1}/MW. For our laser pulse shape this corresponds to broadening of 0.09 and 0.15 cm^{-1} at $P(\langle n \rangle) = 10^{-3}$ and 10^{-1}, respectively, for P_{20} irradiation of ethyl acetate, if the mean intensity in the first 200 ns of the pulse is used to calculate ω_R. An important aspect of the acetate

systems, relative to other carefully documented examples of multiple photon-induced reactions, is the relatively small degree of power broadening because the integrated absorption cross section is rather small. At 700 cm^{-1}, which is about the most probable energy of a room-temperature sample, the majority of states are various combinations of the three torsional modes (80, 130, and 150 cm^{-1}) adding to 700 cm^{-1} plus a few states with one quantum in the $\sim$420-cm^{-1} modes and enough quanta in the torsional modes to give 700 cm^{-1}. Thus, the observed absorption band in a room temperature sample is actually a superposition of hot bands in which molecules in several different states absorb one 1050-cm^{-1} photon. The $\sim$30-cm^{-1} breadth (see Figure 1 of ref 1) of the band is mainly associated with the rotational envelope from these states. In the 2000-cm^{-1} range the state density is $\sim$120 states cm^{-1}, and contribution to the 1050-cm^{-1} absorption band from combination transitions involving changes of quantum numbers of several modes are feasible with respect to energy resonance; however, there is no reason to expect that most of these combination transitions would have high oscillator strength. Nevertheless, combination transitions involving +1 quantum change in the 1150-cm^{-1} group and -1 changes in the torsional modes could contribute to absorption of the first 1050-cm^{-1} photon.

The explanation for the absence of low-energy anharmonic bottleneck during the sequential laser absorption process may be fast intramolecular relaxation following the absorption of one or two photons, or it may be because the two modes of nearly the same frequency plus the large number of frequencies in the 1150–1700-cm^{-1} range provide fortuitous compensation of anharmonic mismatch in the pumped mode. Since the total density of vibrational states following absorption of one and two photons by room-temperature ethyl acetate molecules is $\sim$120 and 10^3 states/cm^{-1}, respectively, rapid relaxation from the pump mode to the internal bath states seems improbable.[29] Therefore, we tend to favor the second explanation. This type of explanation also has been advocated for C$_2$H$_5$Cl;[4] the five nearly degenerate C–H stretch modes were suggested to provide a band of energy states which circumvent the anharmonic shift problems of the pump mode when irradiated at 3 μ. Since a large number of acetates,[1,27] even methyl acetate,[1] have similar $\sigma_L(\phi)$ values, a general explanation for the absence of an anharmonic bottleneck is needed and the detailed spectroscopic properties of ethyl acetate probably will not explain the absence of the anharmonic bottleneck. Since the $\sigma_L(\phi)$ values vary only modestly with ϕ, direct two- or three-photon processes presumably are negligible and the sequential absorption model should be retained. Before proceding further, some understanding of the rotational structure of the band is needed.

In the simplest, but hopefully realistic, view the band resembles a perpendicular transition of a nearly symmetric top. The structure is dominated by the Q branches from different stacks of K levels. These Q branches would be separated by 2(A–B) $\approx$ 0.5 cm^{-1} for ethyl acetate. For a single lower vibrational state the fraction of rotational levels exactly in resonance with a *single* upper vibrational state for pumping frequency of 0.2 cm^{-1} breadth is relatively small and should consist of one stack of K levels plus a limited number of P and R branch transitions from other K stacks. From this point of view, fluence-dependent rotational fractionation is quite understandable and *the large fraction of molecules which not only absorb the radiation but also actually react is the surprising observation.* In contradistinction to this model, no significant structure could be observed in a spectrum taken at 0.05-cm^{-1} resolution. The obvious reason is the overlapping of the transitions of the two 1050-cm^{-1} modes plus any hot-band contribution which also will cause overlapping. Thus, the density of rotational lines is quite high and the $\sigma_L(\phi)$ value at low ϕ should be the same as the broad-band cross section measured at $\sim$1 cm^{-1} resolution. Nevertheless, the high density does not explain how such a very high fraction of molecules, seemingly irrespective of rotational state, can be in resonance with the specific laser frequency. In fact, this is a quite common

(28) George, W. O.; Houston, T. B.; Harris, W. C. *Spectrochim. Acta, Part A* **1974**, *30*, 1035.

(29) Kay, K., private communication, 1981.

occurence for large molecules, and interesting work by Brenner and co-workers[30] with Cl_2CS have conclusively demonstrated that the entire rotational population can be pumped under truly collisionless conditions.

The explanation of the large fraction of molecules which, in fact, do absorb the first photon is more perplexing than the absence of an anharmonicity bottleneck. Perhaps the explanation to both questions has the same origin. To pump all rotational levels of the vibrational states present in a thermal sample, it is necessary to consider the type of vibrational states within ± 10 cm^{-1} of the pumping frequency for a given lower state energy (we used 700 cm^{-1}) that may compensate for lack of rotational energy match for absorption of a single 1050-cm^{-1} photon. Transitions with one quantum change in the 1050-cm^{-1} mode plus changes in no more than two quantum numbers, of low frequency modes, comprise about 5% of the total accessible upper states. If states corresponding to +1 quantum in the 1150-cm^{-1} group plus a reduction of quanta in the low-frequency modes are included, then the number of accessible states increase to 10–15% of the total. The remaining states seem unlikely to have high oscillator strengths because too many quantum numbers must change or a large change in one mode is required. This analysis was done for a single pumped mode. For two pumped modes of nearly the same frequency, as for $CH_3CO_2C_2H_5$, the fraction of accessible states will be increased somewhat. This analysis must be applied to all lower states in a room-temperature sample to get a complete result. The above analysis does suggest that a large fraction of molecules in a thermal sample could absorb energy, providing that a large number (but not necessarily all) of the upper vibrational states are accessible and compensate for rotational mismatch of energy. A puzzling feature of this proposed explanation is the apparent high oscillator strengths of the combination transitions. For Cl_2CS Brenner[30] has suggested that higher order terms need to be included in the transition dipole.

VI. Conclusions

A master equation formulation with stepwise incoherent laser excitation was used for model calculations of multiphoton reaction of a large molecule resembling ethyl acetate. The calculations provide a frame of reference for infrared photochemistry of other molecules with properties resembling ethyl acetate. Steady-state kinetics is only appropriate for very high reaction probabilities, i.e., $P(\phi) \gtrsim 0.8$. For reaction probabilities $\lesssim 0.10$, consideration must be given to postpulse contributions to reaction yields. For laser-initiated reactions which are exothermic or nearly thermal-neutral, recognition must be given to the thermally driven contribution in the irradiated volume prior to dissipation of the energy deposited by the laser to the surrounding cold gas.

Master equation calculations with absorption cross sections that match the energy deposition data for ethyl acetate and ethyl fluoroacetate together with evaluation of postpulse processes showed good agreement with the experimental reaction probabilities for P_{20} irradiation of ethyl acetate and R_{12} irradiation of ethyl fluoroacetate. However, the agreement for $P(\langle n \rangle) \leq 0.1$ was rather poor for P_{10} irradiation of ethyl fluoroacetate and totally inadequate for all reaction probabilities for P_{38} irradiation of ethyl acetate. These difficulties can be explained if fluence-dependent rotational fractionation is added to the model. The postpulse effects can be more easily modeled for experiments in which $P(\langle n \rangle)$ is measured for constant pressure of bath gas. Calculated results with a reasonable choice for a collisional deactivation model, for $CH_2FCOOC_2H_5$ in CF_4, are in good agreement with the experimental data. The level-to-level absorption cross sections deduced from the energy absorption measurements depend weakly on excitation energy and vibrational anharmonic bottlenecking is minimal. The large number of vibrational modes in the 1150–1000-cm^{-1} range together with the low-frequency torsional modes may provide a band of energy states which circumvent the anharmonic shift problems of the pump mode. Explanation of

the very high fractional reaction, nearly unity for high ϕ, requires that all molecules, regardless of rotational state, participate in the multiphoton absorption even though the power broadening, ≤ 0.5 cm^{-1}, is inadequate to explain this. The addition of rotational states to the multiphoton absorption models needs theoretical attention.

Note Added in Proof. Stark shifting of the rotational lines by the strong laser field appears to be one possibility for explaining the absorption by such a large fraction of the rotational levels of the organic esters. For a laser intensity of 2 MW/cm^2, the estimated[9] Stark shift is 0.5–5 cm^{-1}, depending on the rotational quantum numbers of the level in question.

Appendix. I. RRKM Models of Ethyl Acetate

Several different models were explored to estimate the uncertainty in the RRKM rate constants for ethyl acetate. Any model must fit the thermal equilibrium Arrehenius A factor $\sim 10^{12.6}$ s^{-1}. The most important question for the molecule is the description of the four hindered internal rotations in ethyl acetate. The main purpose of this Appendix is to investigate the differences in RRKM rate constants in treating the hindered rotors as torsional vibrations and as free rotors.

Model A. Vibrational Model. Molecular frequencies were assigned for the known frequencies of methyl acetate[28] with replacement of the frequencies of a C–H group by the frequencies of a CH_3 group. Among the 36 vibrations of the molecule, there are 13 stretches and 23 deformations; 4 of the latter are hindered rotational motions. Model A treats these as torsional vibrations and Table I shows the vibrational frequency assignments. The stretches and 19 of the bending modes can be considered as well established, at least for state-counting purposes, and only the four torsions are uncertain. These were assigned by comparison to methyl acetate and other similar molecules.

The frequencies of the transition state were estimated by taking into account the changes associated with forming a six-centered complex. The frequencies that differ from the molecule were the same as those recommended by Benson and O'Neal.[31] The CH_3CH_2 torsion was taken as the reaction coordinate and the changes made in other ethyl acetate frequencies are given in the lower half of Table I. This model with reaction-path degeneracy of 3 gives an entropy change for the reaction of $\Delta S^\ddagger = -6.89$ gibbs mol^{-1}, $A = 10^{12.63}$ s^{-1}, and $E_0 = 47.5$ kcal mol^{-1} for an E_{act} of 48.0 kcal mol^{-1}.

Model B. Free Rotor Model. The torsional motions of ethyl acetate were treated as free rotors except for the oxygen–carbonyl carbon hindered rotor which has a high barrier.[32] In the complex, only the methyl torsion was treated as a free rotor. The symmetry numbers of all free rotors were taken as 1, but the reaction path degeneracy was set equal to 3. the two CH_3 rotors certainly hae symmetry numbers of 3. However, the CH_3 rotor attached to the carbonyl group has the same symmetry number in the molecule and in the trasition state; therefore, the symmetry numbers cancel from the calculations of k_∞ and the RRKM rate constants. The other CH_3 rotor needs more careful consideration. This rotor is involved in the reaction path and the symmetry number is the origin of the reaction path degeneracy, which is set as 3; hence, the symmetry number can be ignored.
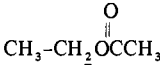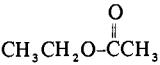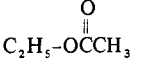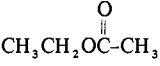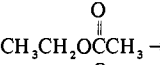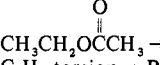
In the first trial the vibrational frequencies of the molecular and activated complex were taken as the same as for the torsional model except for the three torsions for the molecule and one torsion for the complex which become rotors. The moments of inertia of a CH_3 rotor is 3.0 amu Å^2 and that for ethyl is 17.0 amu Å^2 if they are attached to frames of infinite mass. These moments of inertia were corrected to 1.7 and 7.0 amu Å^2 by considering the barrier heights of the internal rotation and the reduction in q_{1R} from the free rotor values. This free rotor model gives $A = 10^{11.92}$ and $E_0 = 46.2$ kcal mol^{-1}; the A factor is lower by a factor

(30) (a) Brenner, D. M.; Spencer, M.; Steinfeld, J. I. *J. Chem. Phys.* **1981**, *75*, 3153. (b) Brenner, D. M. *Ibid.* **1981**, *74*, 2293.

(31) Benson, S. W.; O'Neal, H. E. Report NSRDS-NBS 21; National Bureau of Standards: Washington D.C., 1970.
(32) Dale, J. *Tetrahedron* **1966**, *22*, 3373.

Table I. Molecular and Transition State Frequencies (cm⁻¹)

Molecule: Stretching Modes

(CCH_3, OCH_2) (8)	2956		$C-OCH_2$ (1)	1248
$C=O$ (1)	1741		CH_3-CH_2	1000
$CO-CH_2$ (1)	844		CH_3-CO	1046

Bending Modes

$(CCH_3, OCH_2)_{def}$ (6)	1420		$(CH_2)_R$ (1)	850
$(C-CH_3)_R$ (2)	1106		CH_3-CO_2	607
$(CO-CH_3)_R$ (1)	1036		$O-C-O$ (1)	420
$(CH_3 \text{ and } CH_2)_{W\&T}$ (3)	1385		$C-O-C$ (1)	379
$(CH_3)_R$ (1)	980		$C-C-O$ (1)	442
			$O=C-C$ (1)	463

Torsions

$CH_3-CH_2\overset{\overset{O}{\|}}{O}CCH_3$	150	$CH_3CH_2O-\overset{\overset{O}{\|}}{C}CH_3$	150
$C_2H_5-\overset{\overset{O}{\|}}{O}CCH_3$	80	$CH_3CH_2O\overset{\overset{O}{\|}}{C}-CH_3$	130

Grouped Frequencies

2956 (8)	1442 (10)	1153 (3)	1041 (2)	990 (2)	767 (3)	426 (4)	143 (3)	80 (1)

Changes for the Transition State

$C-H \rightarrow C--H$	2200 (1)		$O=C-O \rightarrow O-C-O$	600 (1)
$C-C \rightarrow C-C$	1300 (1)		$C-O-C \rightarrow C- O--C$	220 (1)
$CO-CH_2 \rightarrow CO--CH_2$	700 (1)		$C-C-O \rightarrow C-C--O$	220 (1)
$C-OCH_2 \rightarrow C-OCH_2$	1400 (1)		$O=C-C \rightarrow O-C-C$	600 (1)
$C=O \rightarrow C-O$	1325 (1)		$CH_3CH_2O\overset{\overset{O}{\|}}{C}CH_3 \rightarrow CH_3--CH_2\overset{\overset{O}{\|}}{C}CH_3$	650 (1)
$H-CH$ (2) $\rightarrow H--C-H$	725 (1)		$CH_3CH_2O\overset{\overset{O}{\|}}{C}CH_3 \rightarrow CH_3CH_2O-\overset{\overset{O}{\|}}{C}CH_3$	450 (1)
$\rightarrow H--C-C$	577 (1)		$C_2H_5\text{-torsion} \rightarrow Rx \text{ coordinate}$	

Grouped Frequencies, cm⁻¹

2862 (8)	1390 (10)	1055 (5)	664 (8)	450 (1)	220 (2) 130 (1)

of 5 than the experimental result.

The activated complex structure is too tight and the torsional $CH_3CH_2OOCCH_3$ and $CH_3CH_2OOCCH_3$ frequencies were lowered from 650 to 400 and from 450 to 200 cm⁻¹, respectively. This gave $A = 10^{12.46}$ s⁻¹, $\Delta S^{\ddagger} = -7.66$ gibbs mol⁻¹, and $E_0 = 45.7$ kcal mol⁻¹. In the third free rotor model the two torsional frequencies were further lowered to 300 and 180 cm⁻¹; this model gave $A = 10^{12.63}$ s⁻¹, $\Delta S^{\ddagger} = -6.90$ gibbs mol⁻¹, and $E_0 = 45.6$ kcal mol⁻¹. Comparison of the k_i values for the best rotor model and model A shows that the free rotor values are higher by ~2 for ≥ 70 kcal mol⁻¹ and by 3.5 for lower energy. We believe that this encompasses the range of uncertainty in rate constants. The increased heat capacity, relative to the molecule, of the free rotor model transition state causes a 1–1.5 kcal mol⁻¹ greater reduction of E_0 relative to the torsional transitional-state model. This is why the ratios of RRKM rate constants for the two models are energy dependent.

Appendix II. Steady-State Regime

The steady state is easily recognized by inspection of a ln (1 − F_i) vs. time plot (Figure 14) for absorption cross-section model b and 300-ns and 2-μs rectangular pulses; F_i is the fraction of reaction at time t during the laser pulse. For a unimolecular reaction d ln (1 − F_i)/dt = $k_{uni}(t)$ and for steady-state; $k_{uni}(t)$ = constant = $k_{uni}(st)$. For multiphoton processes, the steady-state condition[10] requires that the overall laser pumping rate equal the overall unimolecular rate. As can be seen in Figure 14 for $\phi \leq$ 1.2 J cm⁻¹, the steady state is not reached even at the end of the pulse. For $\phi \geq 1.6$ J cm⁻², the steady state is reached (the plots become linear) only for $F_T > 90\%$, and the steady state contribution to the overall reaction yield is very small. The steady-state rate constants obtained from the linear part of the 1 − F_i vs. time plot for absorption cross-section models b and a (not shown) seem to be linear with the laser intensity, which is expected for our model[10b,c] (see Figure 16). The 2-μs pulse data also fit on the line for case b and case a calculations. In other words, $k_{uni}(st)$ linearly depends on the intensity, which shows that the laser
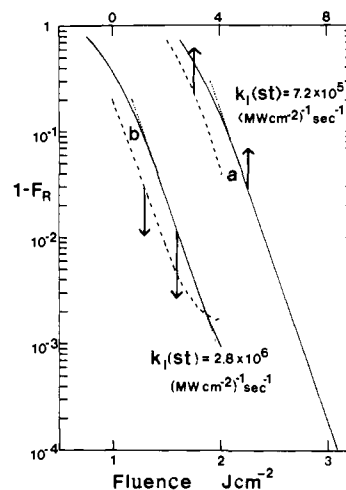

Figure 15. Plot of 1 − F_R vs. fluence for cross-section models a and b, which are defined in Figure 1. The calculations are for collisionless conditions with a 300-ns (—) and 2-μs (···) rectangular pulse. The steady-state rate constant $k_1(st) = k_{uni}(st)/I$ was calculated from the model a and b results using the linear portion of the 300-ns curves; see text.

pumping rate is linearly proportional to the intensity.

Unless time-resolved experiments are made, (1 − F_i) is not a useful parameter. However, since the $k_{uni}(st)$ is linearly proportional to the intensity

$$\frac{d \ln (1 - F_i)}{I dt} = \frac{k_{uni}(st)}{I} = \text{constant} = k_I(st)$$

and

$$\frac{d \ln (1 - F_R)}{I \Delta t_p} = \frac{d \ln (1 - F_R)}{\phi} = k_I(st)$$

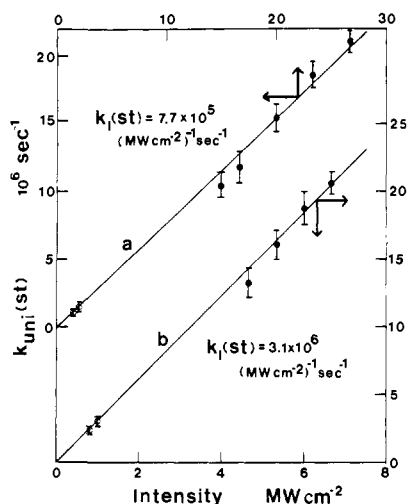**Figure 16.** Plot of $k_{uni}(st)$ vs. intensity for cross-section models a and b: O, 2-μs pulse; 300-ns pulse. The $k_{uni}(st)$ values were calculated from the linear portion of the curves in Figure 14. The slope of this plot provides $k_1(st)$, where $k_1(st) = k_{uni}(st)/I$.

where t_p is the laser pulse length. Therefore, the steady-state region defined with respect to time can be converted to F_R vs. ϕ which are experimentally more useful. The steady-state region is also reached only for $F_R > 80\%$ in the ln $(1 - F_R)$ vs. ϕ plot (see Figure

15). Since $F_R > 80\%$, the postpulse contribution to the overall reaction yield is therefore small and in the steady-state or high-fluence region F_R can be directly related to the experimental reaction yield in a bulb experiment.

The biparticular rate constants,[10] $k_I(st) = k_{uni}(st)/I$, obtained from the linear part of the ln $(1 - F_R)$ vs. ϕ plots are $(0.72 \pm 0.07) \times 10^6$ and $(2.8 \pm 0.3) \times 10^6$ $(MW/cm^2)^{-1}$ s^{-1} for models a and b, respectively. These results may be compared with the values $0.77 \pm 0.03 \times 10^6$ and $3.1 \pm 0.3 \times 10^6$ $(MW/cm^2)^{-1}$ s^{-1} for model a and b, respectively, obtained from Figure 16. The good agreement demonstrates that numerical accuracy is retained for the high fractional reaction necessary to reach steady state. The $k_I(st)$ values do not seem to depend on the intensity. This is very important because experimental plots of ln $(1 - F_R)$ vs. ϕ can be made with data for which time (pulse length) was held constant but intensity varied in order to change fluence. The serious problem of extracting experimental $k_1(st)$ values is the need to accurately measure F_R at very high fractional reaction; the present calculations suggest the limiting slope should be derived from data for which $P(\phi) \geq 0.80$. However, on the positive side, $k_I(st)$ is sensitive to the cross-section model. Thus, $k_I(st)$ is an important experimental measurement.

Indirect Detection of 199Hg NMR: Adducts of Ethylmercury Phosphate with Amino Acids and Ribonuclease

D. A. Vidusek, M. F. Roberts,* and Geoffrey Bodenhausen

Contribution from the Chemistry Department and the Francis Bitter National Magnet Laboratory, Massachusetts Institute of Technology, Cambridge, Massachusetts 02139. Received December 14, 1981

Abstract: 199Hg NMR spectroscopy is used to examine the interaction of the toxic organomercurial ethylmercury phosphate with various amino acids. Because of the relative insensitivity of 199Hg and the low concentrations of biological molecules, a heteronuclear spin-echo and a two-dimensional technique involving a double transfer of polarization are used to bypass the concentration limits of direct detection. The chemical shifts of 199Hg cover a wide range (600 ppm for ethylmercury derivatives) and are diagnostic for the identity of the ethylmercury adduct. Using the mercury chemical shifts and pH stability determined for adducts of the ethylmercuric ion with individual amino acids, we suggest that the ethylmercury–ribonuclease adduct involves modification of the N-terminal lysine residue.

Recent interest in organomercurials is based on their extreme toxicity.[1] Within a cell these compounds may react with proteins, nucleic acids, and even membranes (amino phospholipids). Complexes of organomercurials, typically methylmercury, with the individual components of these macromolecular assemblies have been studied in some detail. While cysteine forms nearly covalent complexes with methylmercury (this is often exploited in forming heavy atom derivatives of proteins with free sulfhydryl groups),[2] nitrogen-bound complexes (histidine, tryptophan, free

amine groups) and much weaker carboxylate complexes can also form.[3] Methylmercury binds to N-3 of uridine and cytidine and to the same site in purine nucleosides and nucleotides.[4] Changes in the sedimentation characteristics of DNA show that methylmercury reacts with the imino (NH) bonds of thymine and guanine[5] as well. More complex model systems, with several different reactive species, have not been examined because most analytical techniques are not selective or sensitive enough to identify the mercury ligand.

(1) (a) Curley, A.; Sedlak, V.; Girling, E.; Hawk, R.; Barthel, W.; Pierce, P.; Likosky, W. *Science* (Washington, D.C.) 1971 *172*, 65. (b) Bache, C.; Gutenmann, W.; Lisk, D. *Ibid.* 1971, *172*, 951. (c) Fridberg, L.; Vostel, J. "Mercury in the Environment; An Epidemiological and Toxicological Appraisal"; CRC Press: Cleveland, OH, 1972.

(2) (a) Banner, D. W.; Bloomer, A. C.; Petsko, G. A.; Phillips, D. C.; Pogson, C. I.; Wilson, I. A. *Nature (London)* 1975, *255*, 609. (b) Tsernoglou, D.; Petsko, G. A. *FEBS Lett.* 1976, *68*, 1.

(3) (a) Simpson, R. *J. Am. Chem. Soc.* 1961, *83*, 4711. (b) Simpson, R. *Ibid.* 1964, *86*, 2059. (c) Libich, S.; Rabenstein, D. *Anal. Chem.* 1973, *45*, 118. (d) Rabenstein, D.; Ozubko, R.; Libich, S.; Evans, C.; Fairhurst, M.; Suvanprakorn, C. *J. Coord. Chem.* 1974, *3*, 263.

(4) (a) Mansy, S.; Wood, T.; Sprowles, J.; Tobias, R. *J. Am. Chem. Soc.* 1974, *96*, 1761. (b) Mansy, S.; Tobias, R. *Ibid.* 1974, *96*, 6874.

(5) (a) Gruenwedel, D.; Davidson, N. *Biopolymers* 1967, *5*, 847. (b) Gruenwedel, D. *Eur. J. Biochem.* 1972, *25*, 544.